

# **TUNABLE MICRO-INTERFEROMETERS FOR TELECOMMUNICATION AND SENSOR APPLICATIONS**

By  
**Jung-sik Moon**

A DISSERTATION SUBMITTED IN PARTIAL FULFILLMENT OF THE  
REQUIREMENTS FOR THE DEGREE OF

MASTER OF SCIENCE  
(MECHANICAL ENGINEERING)

at the  
**UNIVERSITY OF CALIFORNIA, IRVINE**  
2001

© Copyright by Jung-sik Moon 2001  
All Rights Reserved

# Abstract

This thesis studies the performance limitations of MEMS tunable interferometers. MEMS technology offers many advantages, including scalability for wide tuning range in a single device, sensitivity for precision sensing, and batch fabrication capability for cost reduction. However, MEMS technology introduces many new challenges, such as fabrication yield, device reproducibility, and fabrication imperfections, all are factors limiting performance. In addition, tunable interferometers, unlike fixed cavity conventional non-tunable devices, are vulnerable to change in environmental conditions. Although high sensitivity may be beneficial for precision sensors, it is equally disadvantageous due to sensitivity to undesirable perturbations.

In this thesis possible tuning methods suitable for MEMS technology are compared. As a result of wide tuning range, simple fabrication, and versatility, a single-pass plane tunable-cavity Fabry-Perot interferometer was selected as a potential micro-interferometer. In order to characterize device performance principles of an ideal and an imperfect Fabry-Perot interferometer were studied. Performance sensitivity of a single-pass plane tunable-cavity interferometer was studied in the presence of common non-idealities as a result of using MEMS technology. Common imperfections such as accumulative composite misregistration and thermal expansion effects were modeled using Ansys coupled-field finite element analysis (FEA) package, . These results were used to analyze the performance sensitivity of passive MEMS based Fabry-Perot structures. It was concluded that as a result defects limiting performance passive, active feedback control is necessary to achieve high performance required for high end applications. In addition, various suspension designs were proposed for relieving residual stress to prevent the bowing of the

mirror. Future work will involve setting up equipment to measure deflection and parallelism of the Fabry-Perot mirror optically using a modified Michaelson interferometer and observing the changes in performance by adding feedback control for optimal performance.

# Acknowledgements

First and foremost I would like to thank my parents for their support and love throughout the years. As a result of their hard work and dedication for their children, I have been blessed with opportunities they did not have themselves. Also to my three older sisters, who called me “little” brother no matter how old, thank you for everything. To my best friend Jennifer, thank you for believing in me, and putting up with me, without you I would not be a happy person.

I am very much indebted to Dr. Shkel for taking me under his wing and guiding me through not only research, but also my career. He made me appreciate the aspect of continued knowledge, while making me realize my fullest potential. I would like to acknowledge my fellow colleagues in the UCI Microsystems Laboratory for providing a friendly atmosphere and timely discussions, which made this report possible.

# Contents

<b>Abstract</b>	<b>i</b>
<b>Acknowledgements</b>	<b>iii</b>
<b>1 Introduction</b>	<b>1</b>
1.1 Problem Statement . . . . .	1
1.2 Applications . . . . .	4
1.3 Tunable Interferometers . . . . .	6
1.4 Prior Work . . . . .	7
1.5 Thesis Outline . . . . .	9
<b>2 Fabry-Perot Principle</b>	<b>10</b>
2.1 Ideal Fabry-Perot Interferometer . . . . .	10
2.2 Imperfect Fabry-Perot Interferometers . . . . .	13
<b>3 Modeling</b>	<b>18</b>
3.1 1-DOF Mass-Spring System . . . . .	18
3.2 Kinematics of 3-DOF Plate . . . . .	20
3.3 Suspension Modeling . . . . .	22
3.4 Modeling Performance Limits of a Fabry-Perot Filter . . . . .	23
3.4.1 Misregistration . . . . .	23
3.4.2 Thermal Expansion . . . . .	24
3.5 Conclusion . . . . .	25
<b>4 Fabry-Perot Filter Design</b>	<b>29</b>
4.1 MUMPs Surface Micromachining Process . . . . .	29

4.2	Design of Fabry-Perot Interferometers using MUMPs Technology . .	30
4.3	Designs of an Experiment . . . . .	32
4.4	Conclusion . . . . .	32
<b>5</b>	<b>Procedure for Testing</b>	<b>35</b>
<b>6</b>	<b>Conclusion</b>	<b>37</b>
6.1	Future Work . . . . .	38
	<b>Bibliography</b>	<b>39</b>
<b>A</b>	<b>Matlab Codes</b>	<b>42</b>
A.1	intensity.m . . . . .	42
A.2	finesse.m . . . . .	42
<b>B</b>	<b>Ansys Codes</b>	<b>43</b>
B.1	Coupled-Field Finite Element Analysis . . . . .	43
B.1.1	electrostatic.txt . . . . .	43
B.1.2	thermal.txt . . . . .	46
B.2	Stiffness Analysis of Suspension Designs . . . . .	48
B.2.1	beam.txt . . . . .	48
B.2.2	single.txt . . . . .	49
B.2.3	double.txt . . . . .	50
B.2.4	parallel.txt . . . . .	51
B.2.5	tune.txt . . . . .	52
<b>C</b>	<b>L-Edit Layout</b>	<b>54</b>
C.1	Labeling . . . . .	54

# List of Figures

1	(a)Classical discrete approach requires a collection of etalons, each responsible for a specific wavelength. (b)An array of etalons are replaced by a single variable cavity interferometer. . . . .	2
2	(a)Fine tracking of high-density optical data storage. (b)Actuation of the micro-mirror resulting in fine tracking distance of $d$ . . . . .	5
3	Four possible tuning methods for interferometry. . . . .	7
4	Light passing through two partially transmitting parallel mirrors A and B separated by a cavity length $d$ filled by a medium with index of refraction $\mu$ . . . . .	10
5	Interferometer's transmission profile and notions defining device performance. . . . .	14
6	Reflectivity finesse defines performance of a Fabry-Perot interferometer, under ideal conditions (i.e. Perfectly flat mirrors). In practice a Fabry-Perot interferometer is non-ideal, and it's performance is defined by the effective finesse, where it asymptotically reaches a limit determined by the defect finesse. . . . .	15
7	(a)Classification of plate defects (adopted from Atherton). (b)Fringe broadening effect as a result of convolution of the Airy function and parallel deviation surface defect. . . . .	16
8	(a)Simplified model consist of a $100\mu m \times 100\mu m$ mirror suspended by four beams ( $8\mu m$ wide, $2\mu m$ thick, $60\mu m$ long) on four corners and a $100\mu m \times 100\mu m$ electrode placed under the suspended mirror, separated by an air filled $2\mu m$ optical cavity. (b)Mass-spring model of an electrostatically actuated Fabry-Perot interferometer. . . . .	19



9	A flat plate with three degrees of freedom. . . . .	21
10	(a)Suspension design. (b)Force load in $y$ . (c)Pressure load in $z$ . . . . .	26
11	An example of mask misregistration during surface micromachining.	27
12	(a)A reduction in effective finesse as a result of even electrostatic pressure on the suspended mirror caused by component misregistration. (b)Fringe broadening effect as a result of even electrostatic pressure on the mirror caused by component misregistration. . . . .	27
13	(a)A reduction in effective finesse caused by thermal expansion. (b)Fringe broadening effect as a result of thermal expansion. . . . .	28
14	MUMPs technology uses a two polysilicon structural layer fabrication process. . . . .	30
15	(a) <i>Poly1 + Poly2 + Metal</i> forming a $2\ \mu m$ gap. (b) <i>Poly2 + Metal</i> supported by ring of <i>Poly1</i> connected to the suspensions forming a $2.75\ \mu m$ gap. . . . .	31
16	(a)Single serpentine passive suspension. (b)Double serpentine passive suspension. (c)Parallel passive suspension. (d)Tunable active suspension	32
17	Identification tags for the Fabry-Perot design and electrodes for the mirror and tuning suspensions. . . . .	33
18	(a)SEM close-up of a double serpentine suspension. (b)SEM of a Fabry-Perot filter with parallel suspension. (c)SEM close-up of an active tune suspension. . . . .	34
19	(a)SEM of an array of micromachined Fabry-Perot interferometers. (b)SEM of a micromachined Fabry-Perot interferometers with serpentine suspensions. . . . .	34
20	Modified Michaelson interferometer for deflection measurement . . .	36

21	Future work will involve setting up a feedback system to increase performance. Fiber to fiber alignment device in conjunction with a collimating lens, laser, fiber, and a spectrometer can be used for measuring the transmitted intensity of micro Fabry-Perot interferometers. Using the quadrant detectors as feedback, we can analyze performance improvement from the optical spectrum analyzer. . . .	38
22	Reading the identification address. . . . .	55
23	Layout for MUMPs run 39. . . . .	56
24	Bonding pad labels. . . . .	57

# Chapter 1

## Introduction

In this chapter the problem statement explains the motivation and challenging problems facing tunable micro interferometers. This section is followed by a discussion on various application for tunable micro interferometers to fully appreciate the versatility of the device. Then, prior work on micromachined Fabry-Perot interferometers is presented. Finally, the chapter is concluded by an outline of the following chapters.

### 1.1 Problem Statement

Plane Fabry-Perot interferometer is made of two partially transmitting parallel plates with a reflective coating forming an optical resonating cavity. Light enters the cavity through one of the mirrors, propagates through the cavity and exits through the other mirror. The transmitted wavelength is a function of the refractive index of the medium, incident light angle, and the length of the optical cavity. As a result of this dependence, this remarkably simple device has enormous applications in sensor and telecommunication industry.

Classical wavelength interferometers are a collection of hand assembled etalons, consisting of two semi-transparent mirrors separated by a fixed-cavity. Individual etalons are designed with a different cavity size, each responsible for filtering a specific wavelength. In Fig. 1(a) light source enters a two-way amplitude divider (composed of light rotator with a port to the light source, etalon, and the subsequent amplitude divider [1]) and propagates through the rotator and into

etalon 1, passing  $\lambda_1$ , while reflecting  $\lambda_2, \lambda_3, \lambda_4, \dots, \lambda_N$  back through rotator and into the subsequent rotator. This process is repeated until the desirable wavelengths are filtered. Consequently, this method of wavelength tuning requires an array of etalons, which can get quite expensive. For example, a 40-channel interferometer, at \$300 per etalon, can cost \$12,000.

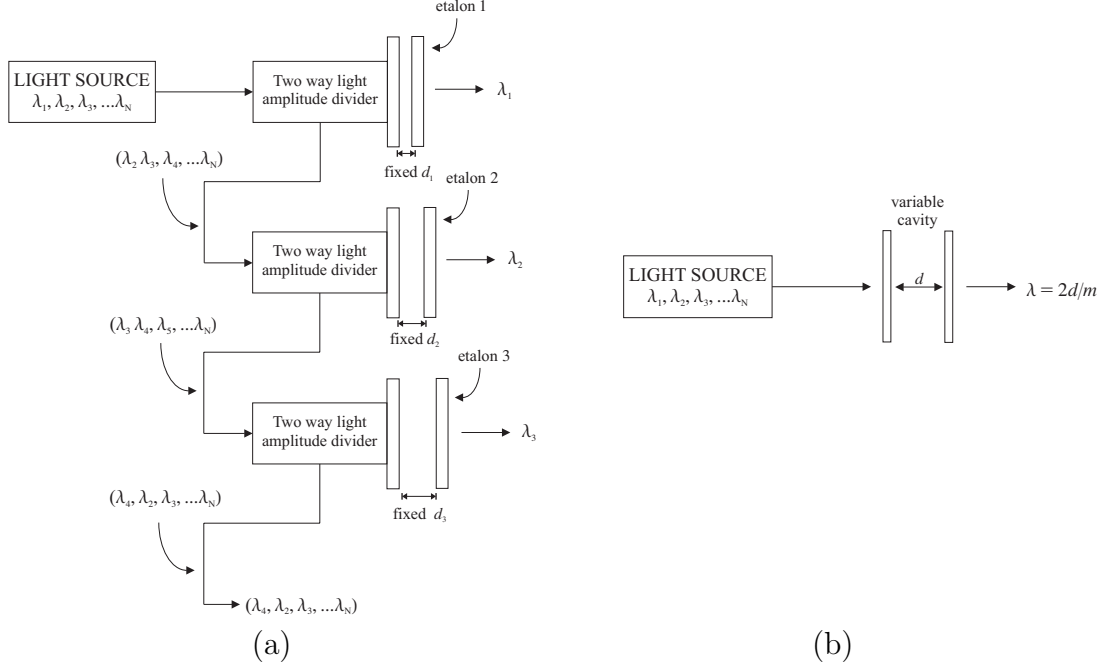


Figure 1: (a) Classical discrete approach requires a collection of etalons, each responsible for a specific wavelength. (b) An array of etalons are replaced by a single variable cavity interferometer.

An alternative to a classical wavelength interferometer (an array of hand-assembled etalons consisting of two semi-transparent mirrors separated by a fixed-cavity) is the implementation of wide band tunable filter using Micro-Electro-Mechanical Systems (MEMS) technology. This approach will allow a single tunable device to replace an array of fixed-cavity filters reducing cost and parts, illustrated in Fig. 1(b). In addition, MEMS technology offers many other advantages, including scalability for wide tuning range, sensitivity for precision sensing, and batch fabrication capability for cost reduction.

However this transition is not simple, MEMS technology introduces many new challenges, which include fabrication yield, device reproducibility, and fabrication imperfections - all are factors seriously limiting performance of MEMS interferometers. Also, tunable devices are sensitive to external factors, e.g. temperature, pressure, and acceleration fluctuations, whereas fixed devices are less sensitive. Furthermore, high reflectivity values necessary for high performance require coating the mirror's surface with quarter-wavelength dielectric films, but comes at a tradeoff because the additional dielectric layers introduces defects. Fabry-Perot interferometers are very sensitive devices, and deviations from perfectly flat, smooth, or parallel surfaces are the causes to limited performance, even at very high reflectivities. In practice, non-idealities in fabrication techniques or sensitivities to environmental condition lead to parameter variations, ultimately degrading performance. For example, curvature of the mirror, non-parallelism of the mirror, perturbation of the mirror, and non-isotropic suspensions arise from residual stress, gradient stress, accumulative composite misregistration, non-uniform etching, and external environmental fluctuations. Little work have been done in analyzing and compensating performance loss of interferometers using MEMS technology. Therefore, the goal of this thesis are:

- Explore potential for using tunable devices.
- Investigate opportunities for implementing device using MEMS technology.
- Analyze performance limits of micro-machined tunable devices and propose methods for improvement.
- Design and fabricate MEMS interferometers.

## 1.2 Applications

Amazingly enough, a simple device consisting of two parallel partially transmitting mirrors can perform a wide variety of functions. There are many applications for Fabry-Perot interferometers, but coupled that with MEMS technology, suddenly applications for micro-Fabry-Perot interferometers are endless. This section highlights a few examples.

Monitoring the intensity of the transmitted beam while holding the light source constant, many sensing applications are realized. For example, micro pressure sensors can be used on compressor or turbine blades for understanding unsteady pressure oscillations in fan blade fatigue [2]. If the optical cavity has a reference pressure (i.e. vacuum), any change in pressure outside of the optical cavity will result in a change of cavity gap, thus shifting the maximum transmitted intensity proportional to the change in length. Assuming a relationship between the cavity gap and the pressure change is known, the change in the intensity profile is used to calculate the pressure outside. Similarly acceleration, temperature, and strain all alter the cavity length, and are sensed just similarly. Chemical sensing is also possible since the refractive index, like the cavity length is directly proportional to shift in the maximum transmitted intensity. Potential applications of micro Fabry-Perot sensors are seemingly endless, since these devices can be embedded into biological systems, building, or in places thought too small for current sensors to reach. It is possible with appropriate integrated control electronics and packaging, a single micro Fabry-Perot can replace a family of sensors in a single device!

Although tuning of wavelengths can be achieved by actuating one of the optical mirrors, it is not limited as an interferometer. By simply adding a reflecting coating on the outer surface of the actuated mirror, it can now be used as a micro-mirror. For example, controlling the position of the pickup probe well below the track pitch is critical for high-density data storage. Using a micro-mirror for fine tracking laser

beam for high-density optical data storage, allow precise positioning, fast response, and non-contact method result in faster tracking speed [3]. Fig. 2(a) is a picture of a fine tracking of a high-density optical data storage, and a close up the fine tracking and pickup system. The micro-mirror is mounted at a 45 degrees to the laser source, and the actuation of the micro-mirror out of plane with distance  $h$  result in the fine tracking of the optical disk related by  $d = \sqrt{2}h$ , Fig. 2(b).

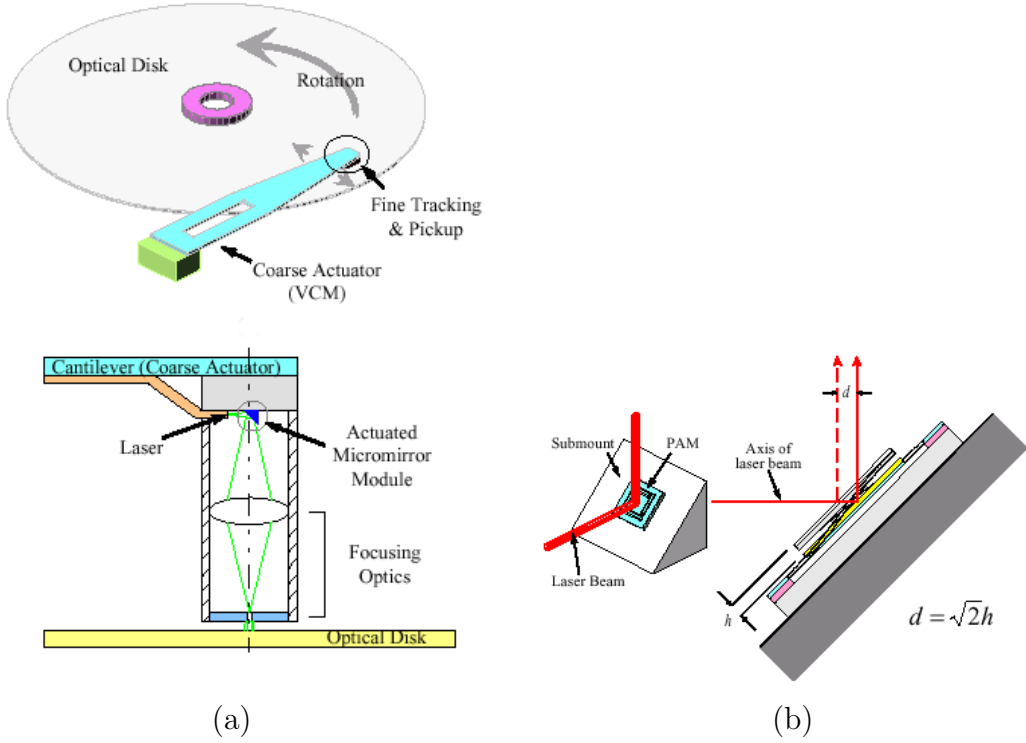


Figure 2: (a)Fine tracking of high-density optical data storage. (b)Actuation of the micro-mirror resulting in fine tracking distance of  $d$ .

Growing demand in the data communication has given rise to Dense Wavelength Division Multiplexing (DWDM). Even with the increase of data rates in a fiber optic cable from  $2.5 \text{ Gb/s}$  to  $10 \text{ Gb/s}$ , higher data rates are still in demand. DWDM technology allows the transmission of multiple channels in a single fiber optic line, thus increasing the data. Currently, operational wavelengths standard for telecommunication uses the ITU-T standard wavelengths

of 1528.77 nm to 1560.61 nm with 0.49 nm channel spacing to get 81 channels  $((1560.61 \text{ nm} - 1528.77 \text{ nm})/0.49 \text{ nm} - 1 = 81 \text{ channels [4]})$ . These wavelengths were selected because they corresponds to wavelengths that undergo the least attenuation in optical fibers, and it also corresponds to the band of wavelengths amplified in erbium-doped fiber amplifiers (EDFAs) [5]. Transmission of 81 channels significantly increases the data rates from 10 Gb/s to 810 Gb/s. Applications of micro Fabry-Perot interferometers are multiplexing, demultiplexing, channel monitoring systems for monitoring and tracking of all wavelengths, and maintenance.

Other applications for micro-Fabry-Perot interferometers include tunable laser source [6], displays, and telescopes, microscopes, and spectrum analyzers.

### 1.3 Tunable Interferometers

Four possible tunable filters are presented in Fig. 3, they include diffraction grating filter, tunable cavity interferometer, variable angle etalon, and “linear sliding” Fabry-Perot interferometer. Diffraction grating filter induces interference through the grating surface, and tuning is achieved by rotation (changing the incident beam angle) [7]. Tunable cavity interferometer is a Fabry-Perot interferometer (FPI), where incident beam enters the cavity normal to the mirrors, and a light wave of selected frequency resonates through interference. The resonating cavity length equals multiples of half wavelength, and tuning is achieved by changing the cavity length. Similarly, the variable angle etalon is a Fabry-Perot interferometer, but with a fixed cavity. Rather than varying the cavity length, tuning is achieved by changing the incident beam angle. The resonating condition for an etalon is met when the cavity length equals multiples of half wavelength divided by cosine of the angle measured from the mirror normal. Finally, the “linear sliding” filter operates like the tunable cavity filter, but the cavity length is varied by sliding the tapered surface.



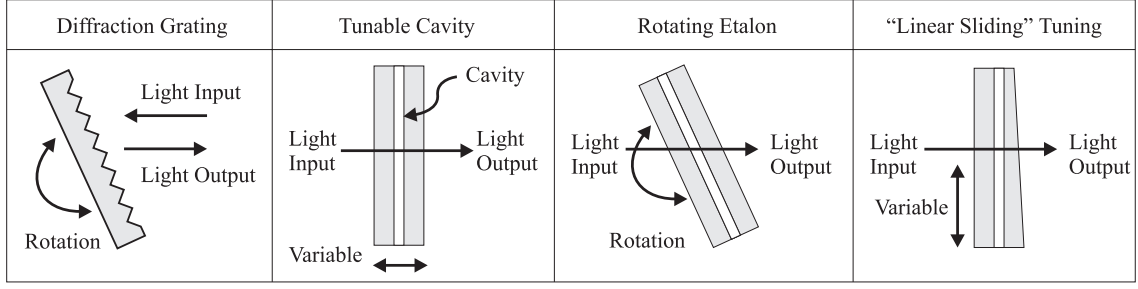


Figure 3: Four possible tuning methods for interferometry.

Diffraction grating filter is capable of having a wide tunable range, but high polarization is a problem. Likewise, rotating etalon has high polarization dependence and characteristics change as a result of changing incident beam angle, while tuning. Although, stability and reliability of a rotational etalon filter are good, it has limited tuning range. “Linear sliding” filter is stable/reliable, has low polarization dependence loss, and has constant characteristics over the whole tuning range. However, special fabrication techniques are needed in order to generate the tapered surface. While exploring available tuning methods suitable for micromachining technology, wide tuning capability, low polarization, and reduced processing steps made tunable-cavity Fabry-Perot interferometer most attractive.

## 1.4 Prior Work

The first tunable micromachined Fabry-Perot interferometer was invented by Jerman [8] in 1990, and later reprinted in 1991 [6]. The device was fabricated by bonding two silicon wafers with highly reflective multi-layer dielectric mirrors with high and low refractive index forming an optical cavity equaled to  $24\ \mu m$ . Mirror reflectivity ranged from 95 % at  $1.3\ \mu m$  to 97.5 % at  $1.55\ \mu m$ . Wavelength tuning and parallelism of the device was electrostatically actuated by having one wafer with matching set of four control electrodes, and the other wafer suspended by a corrugated diaphragm suspensions. Advantages of corrugated suspension were

increased linear travel, isolation from case stresses, and resistance to off-axis bending. As a result of high refractive index of 3.5 of the silicon substrate, antireflection coatings were utilized on the external surfaces to avoid high Fresnel reflection loss. The parallelism of two surface were observed by using a monochromatic infrared source and TV camera. Misalignment after fabrication was in the order of  $10^{-2}$  degrees, with appropriate bias voltage to the control electrodes parallelism was improved better than  $3 \times 10^{-4}$  degrees. The device exhibited a free spectral range (FSR) of 49 nm near 1550 nm with finesse of approximately 40, allowing to separate 15 channels.

In 1996, Lin [9] proposed a three-dimensional Fabry-Perot etalon using surface micromachining technique and monolithically integrated with an on-chip rotation stage for angle tuning. Rather than restricting the incident beam normal to the surface substrate, a three-dimensional Fabry-Perot etalon made fiber-to-fiber coupling easily acceptable, and provided integratibility with other micro-optical elements easier. 45 nm tuning range at 1.3  $\mu m$  wavelength was achieved for rotation of 70 degrees. Initially, with one side of polysilicon coated with a thin layer of Au lead to finesse of 4.1, with dielectric coating it increased to 11.

In 1997 Peerling [10] realized that a small resonating cavity gap of only a few microns lead to huge spectral range and large bandwidths, which makes transmission of 20-channels with 2 nm channel spacing impossible. He explains that a free spectral range (FSR), or the tuning range does not have to be over 42 nm to transmit 20-channels effectively. In fact, increasing the FSR only instigates the selection of multiple channels. As was concluded in [10], increasing the cavity length to 30  $\mu m$ , and electrostatically tuning over a range of 103 nm with 35 V near 1550 nm, a finesse of 46.6 with bandwidth of 1.2 nm allows the 2 nm channel spacing.

Tayebati [11] in 1998 described the first microelectromechanical tunable filter device with a half symmetric cavity structure. He was able to get 70 nm tuning

with bandwidth of less than  $0.27\text{ nm}$ . The bottom mirror is made by depositing eight pairs of  $\text{SiO}_2$  quarter-wave stack by ion-beam sputtering on a silicon substrate. A sacrificial layer consisting of polyimide is used to form the resonating cavity. The top mirror is made of seven and half pairs of  $\text{SiO}_2/\text{TiO}_2$  by selective deposition. By controlling the stress of the top quarter-wave stack layers, approximately  $310\text{ }\mu\text{m}$  radius of curvature of the mirror is achieved after sacrificial layers were removed, creating a stable resonating cavity. This strategy enabled efficient coupling to standard single-mode fiber without the use of lenses. Thus reducing complexity of packaging for availability in the commercial market. However, yield was a big issue in this device because high precision matching of surface curvature is required.

## 1.5 Thesis Outline

Thesis is divided into four topics: principles of an ideal and non-dial Fabry-Perot interferometer discussed in Ch. 2, followed by modeling performance limitations resulting from component misregistration and thermal expansion in Ch. 3, implementation of design is presented in Ch. 4, and procedure for testing devices in Ch. 5 concludes the work. Conclusion and future work are summarized in Ch. 6.

## Chapter 2

# Fabry-Perot Principle

This chapter presents the principle operation of an ideal and imperfect single-pass plane Fabry-Perot interferometer.

### 2.1 Ideal Fabry-Perot Interferometer

The transmitted rays are focused onto a screen, where they interfere either constructively or destructively.

A Fabry-Perot filter (FPF) is a device that transmits a selected wavelength or frequency by interference of multiple beams through a reflective cavity of length  $d$  formed by two flat, partially transmitting, parallel mirrors separated by a medium of refractive index  $\mu$ , Fig. 4 [12].

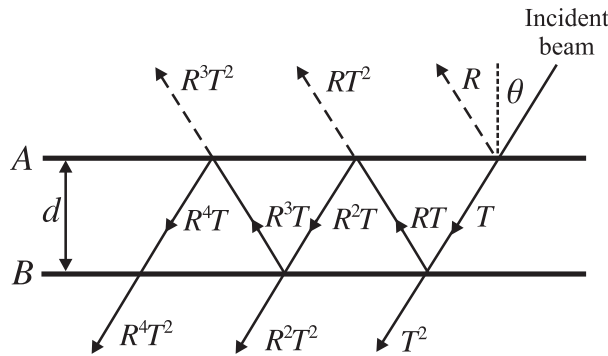


Figure 4: Light passing through two partially transmitting parallel mirrors A and B separated by a cavity length  $d$  filled by a medium with index of refraction  $\mu$ .

Incident beam is reflected and refracted at surface A with an angle  $\theta$  normal to the mirror's surface. Assuming there is no absorption and surface A and B have the

same transmission  $T$  and reflection  $R$  coefficients, fractions of the beam is reflected and transmitted accordingly. The parallel rays of intensity  $T^2, R^2T^2, R^4T^2, etc$  have constant phase lag  $\delta$  between successive beams such that [12]

$$\delta = \frac{2\pi}{\lambda} 2\mu d \cos \theta \quad (2.1)$$

The incident light within the optical cavity undergoes multiple reflections and transmit parallel beams. Once these beams are brought into focus individual wavelengths interfere constructively or destructively. Wavelengths in phase interfere constructively and wavelengths out of phase interfere destructively. The constructive wavelength resonates, at which point the maximum intensity  $I_{max}$  is satisfied when the following expression holds[8]:

$$\mu d \cos \theta = \frac{m\lambda}{2} \quad (2.2)$$

where  $\lambda$  is the wavelength and  $m$  is the fringe order number. For normal incident light with air as the medium ( $\mu = 1$ ), the resonating cavity equals multiples of a half wavelength. Resonating light is analogous to a mechanical system operating on the resonance principle. When the resonance conditions are met, a selected portion of the light spectrum resonates and escapes the Fabry-Perot cavity.

The total transmitted amplitudes are the sum of the amplitudes of the individual beams with success phase shifts. After some derivation, the transmitted intensity  $I$  under ideal conditions is given by the Airy function [12]

$$I = \frac{T^2}{(1 - R)^2} \times \frac{1}{1 + \{4R/(1 - R)^2\} \sin^2 \frac{1}{2}\delta} \quad (2.3)$$

When the quantity  $\sin^2 \frac{1}{2}\delta$  equals 0 and 1,  $I$  is at it's maximum and minimum values, respectively. When  $\sin^2 \delta = 0$ ,

$$I_{max} = \frac{T^2}{(1 - R)^2}$$

If there is no absorption,  $I = T + R$  and  $I_{max} = 1$ . This means that the maximum transmission intensity is equaled to the incident light regardless of the

$R$  and  $T$ . However, if absorption is present at the reflecting surfaces  $I = A + T + R$ , then

$$I_{max} = \frac{T^2}{(T + A)^2}$$

It is also important to note that the ratio

$$I_{max}/I_{min} = \left( \frac{1 + R}{1 - R} \right)^2$$

remains constant regardless of absorption. Therefore, the shape of the transmission is unaffected by absorption. The Airy function can be simplified as,

$$I = \frac{I_{max}}{1 + F \sin^2 \frac{1}{2} \delta}, \quad (2.4)$$

$F$  is called the 'coefficient of finesse', not to be confused with finesse, it is also referred to as the  $F$  parameter,

$$F = \frac{4R}{(1 - R)^2}$$

Examination of Eq. 2.4 reveal the potential of Fabry-Perot interferometers. By taking advantage of parameters such as cavity length, incident beam angle, and the refractive index, Fabry-Perot interferometers exhibit versatility and performance unmatched by no other devices. Not only can it be used as precision actuators for various light modulation application, but also be used to make optical measurements for many high precision sensors. Pressure, strain, chemical, acceleration, and temperature can all be measured by the transmitted intensity.

Finesse is a figure of merit for defining the performance of a Fabry-Perot filter, determining the number of channels or fringes it can transmit effectively. A high finesse value results in sharper transmission peaks and narrow bandwidth, increasing the resolution and allowing additional channels for greater data density. Therefore, understanding factors affecting finesse of a filter is crucial in defining the performance limits.

Wavelength between consecutive interference fringes is called the free spectral range  $FSR_R$  written as,

$$FSR_R = \frac{\lambda^2}{2dn}, \quad (2.5)$$

and full width of the transmittance curve at half of the maximum intensity is called the full width half maximum ( $FWHM_R$ ) defined as,

$$FWHM_R = \frac{\lambda(1 - R)}{n\pi\sqrt{R}}, \quad (2.6)$$

then reflectivity finesse  $F_R$  is defined as the ratio of the free spectral range over the full width half maximum[8]:

$$F_R = \frac{\pi\sqrt{R}}{(1 - R)} \quad (2.7)$$

The physical definition of  $F_R$  is the ratio of tuning range  $FSR_R$  over the half width  $FWHM_R$  a channel, which defines the number of channels or wavelengths it can filter effectively for an idealized system. Reflectivity finesse  $F_R$  is only dependent on the reflectivity of the mirrors, assuming that both mirrors have equal reflectivity. If mirror reflectivity is different, simply replace  $R$  with  $\sqrt{R_A R_B}$ . Intuitively, increasing the reflectivity increases the finesse. However, it will be shown in Sec. 2.2 that mirror defects limit practical values of reflectivity. Fig. 5 is an illustration of an interferometer's transmission profile through several fringe orders or transmission peaks with notations for defining performance. An ideal Fabry-Perot interferometer has sharp transmission peaks, and small bandwidths, whereas the non-ideal Fabry-Perot interferometer has wider bandwidth, reducing the finesse.

## 2.2 Imperfect Fabry-Perot Interferometers

A good description of the applications, history, and theory of Fabry-Perot interferometer is given by Vaughan [13]. He discuss everything from multi-layer dielectric

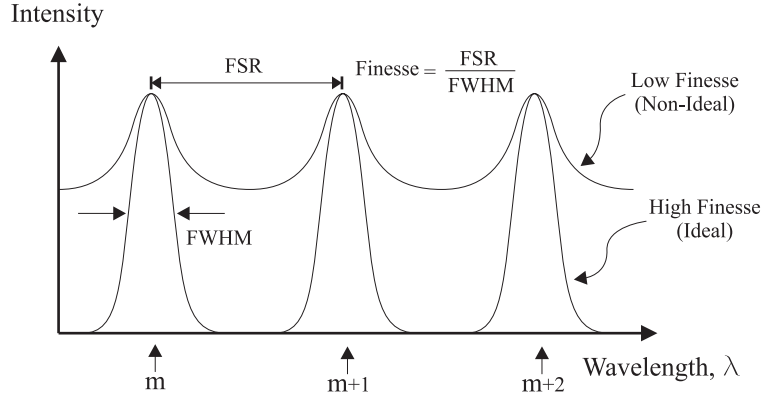


Figure 5: Interferometer's transmission profile and notions defining device performance.

films to analysis imperfect interferometers. Steel talks about multiple-beam interferometers [14]. Introduction of interferometers is given by Tolansky [15]. A good survey for calculation of effective finesse is given by Palik [16] and Sloggett [17]. Modeling of residual stress and stress gradient in the structure causing mirror curvature was studied by Min [18].

In practice, effective finesse  $F_E$ , it is also referred to as instrumental finesse  $F_I$ , of a Fabry-Perot filter is measured empirically, and reflectivity finesse is calculated from Eq. 2.7. Using these results, the defect finesse  $F_D$  is deduced from the following equation [3]:

$$\frac{1}{F_E^2} = \frac{1}{F_R^2} + \frac{1}{F_D^2} \quad (2.8)$$

Fig. 6 is an example which illustrates the defect finesse as the limiting condition for achieving high finesse. The defect in this example assumes parallelism error ( $\delta_p$ ) of  $20nm$ .

The real Fabry-Perot filter's performance is limited by the mirror's imperfections and reflectivity. One common approach for modeling defects is by projecting all surface defects to one reflective surface, considering the other mirror perfectly flat, and convoluting the surface aberrations and the Airy function, Eq. (2.4). This technique assumes that the non-ideal mirror is a collection of infinitesimal



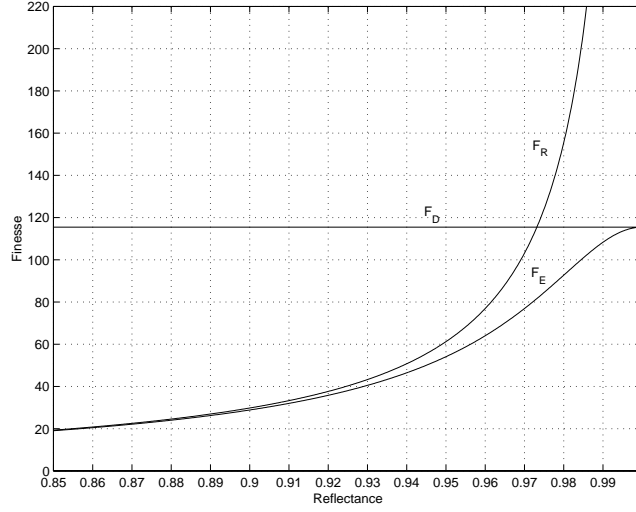


Figure 6: Reflectivity finesse defines performance of a Fabry-Perot interferometer, under ideal conditions (i.e. Perfectly flat mirrors). In practice a Fabry-Perot interferometer is non-ideal, and it's performance is defined by the effective finesse, where it asymptotically reaches a limit determined by the defect finesse.

perfectly parallel mirrors with variable cavity lengths, and the integration over elemental mirrors weighed by a distribution function results in the transmission profile of the non-ideal surface[19]. Three distinct types of defects are used to model plate defects and are illustrated in Fig. 7(a), which is discussed by Atherton [20].  $\delta_p$  is the circular aperture (parabolic error),  $\delta_s$  is the square aperture (parallelism error), and  $\delta_{rms}$  is the surface irregularities following the Gaussian distribution surface, where defects are measured from the planar reference. An illustration of the convolution of a parallelism error can be seen in Fig. 7(b). It is important to note that the instrumental finesse  $F_D$  does not measure individual defect finesse, therefore contribution of each defects are difficult to decouple from empirical results.

Using results derived from Atherton[20], defect finesse due to departure from parallelism, spherically bowed plates, and surface irregularities is given by

$$F_p = \frac{\lambda}{3^{\frac{1}{2}} \delta_p}$$

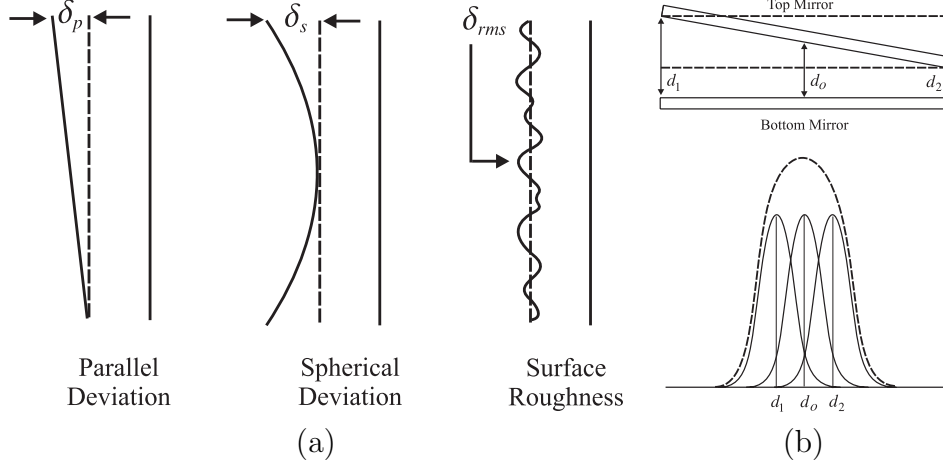


Figure 7: (a) Classification of plate defects (adopted from Atherton). (b) Fringe broadening effect as a result of convolution of the Airy function and parallel deviation surface defect.

$$F_s = \frac{\lambda}{2\delta_s}$$

$$F_{rms} = \frac{\lambda}{4.7\delta_{rms}}$$

where  $\delta_p$  and  $\delta_s$  are the parallel and spherical deviations from a planar reference, and  $\delta_{rms}$  is the root-mean-square deviation following a Gaussian distribution. Representing all three defects simultaneously yields[21]

$$F_D = \left[ \frac{1}{F_p^2} + \frac{1}{F_s^2} + \frac{1}{F_{rms}^2} \right]^{-\frac{1}{2}} = \frac{\lambda}{(3\delta_p^2 + 4\delta_s^2 + 22\delta_{rms}^2)^{\frac{1}{2}}} \quad (2.9)$$

Once  $F_D$  is known,  $F_E$  is calculated by substituting Eq. (2.9) into Eq. (2.8). Generally, a good approximation of  $F_E$  is made with the assumption that imperfect mirrors have defects which are Lorentzian, and  $F_D > F_R$ . Analogous to Eq. (2.7), the notion of effective reflectivity  $R_E$  is corresponding to the effective finesse  $F_E$  is given by the following relationship,

$$F_E = \frac{\pi\sqrt{R_E}}{1 - R_E} \quad (2.10)$$

Using the effective reflectivity found in Eq. 2.10, the transmission function  $I(\lambda)$

of an imperfect etalon is defined as,

$$I(\lambda) = I_{max} \left[ \frac{(1 - R_E)^2}{1 + R_E^2 - 2R_E \cos(2\pi m)} \right] \quad (2.11)$$

where the transmission peak,

$$I_{pk} = \left( 1 - \frac{A}{1 - R} \right)^2 \left( \frac{1 - R}{1 + R} \right) \left( \frac{1 + R_E}{1 - R_E} \right)$$

# Chapter 3

## Modeling

In this chapter a 1-degree of freedom (1-DOF) mass-spring system in static equilibrium is modeled, followed by kinematics for a 3-DOF plate. Ansys finite element analysis (FEA) for various suspension designs and for component misregistration and thermal expansion were performed to model performance limitations of Fabry-Perot interferometers.

### 3.1 1-DOF Mass-Spring System

A solid model of a plate suspended by four suspension beams with electrode are shown Fig. 8(a). Fig. 8(b) is a 1-DOF mass-spring system model. Table 1 is a list of mechanical properties and dimensions used for modeling device in Fig. 8(a).

Assuming deflection is approximately ten times smaller than geometry of the suspension, the restoring force  $F_s$  of the mass-spring system is a linear model,

$$F_s = -kx \quad (3.12)$$

Here the stiffness  $k$  is equivalent to the springs with  $k_{beams}$  and  $k_{plate}$  in series, subscripts denoting stiffness for the beams and the plate. Springs in series is written as,

$$\frac{1}{k} = \frac{1}{k_{beams}} + \frac{1}{k_{plate}}$$

where the beam stiffness  $k_{beam}$  is simply the sum of four guided end cantilever

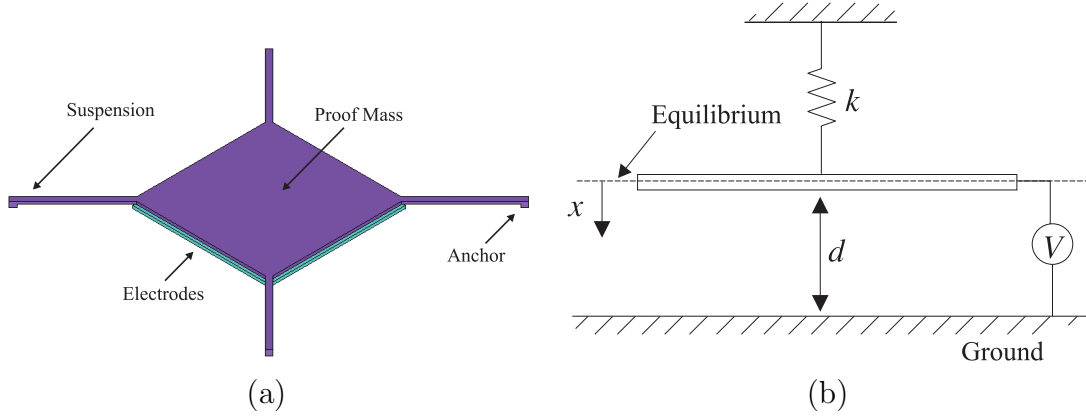


Figure 8: (a) Simplified model consist of a  $100\mu m \times 100\mu m$  mirror suspended by four beams ( $8\mu m$  wide,  $2\mu m$  thick,  $60\mu m$  long) on four corners and a  $100\mu m \times 100\mu m$  electrode placed under the suspended mirror, separated by an air filled  $2\mu m$  optical cavity. (b) Mass-spring model of an electrostatically actuated Fabry-Perot interferometer.

beams [22],

$$k_{beams} = \frac{4Ehw^3}{L^3}$$

and the stiffness of the plate  $k_{plate}$  was calculated with Ansys FEA analysis by fixing four corners of the mirror and applying a pressure over the surface to calculate the displacement.

Electrostatic force between capacitor plates is written as,

$$F_e = \frac{\epsilon_o AV^2}{2(d-x)^2} \quad (3.13)$$

At static equilibrium

$$\vec{F}_e + \vec{F}_s = 0 \quad (3.14)$$

Substituting Eq. 3.12 and Eq. 3.13 in Eq. 3.14, and solving for  $V^2$ , the equation reduces to

$$V^2 = \frac{8Ehw^3}{\epsilon_o AL^3} (d-x)^2 x \quad (3.15)$$

Table 1: Mechanical properties and dimensions of device in Fig. 8

Mechanical Properties of Polysilicon	Young's modulus ( $MPa$ )	$1.7 \times 10^5$
	Poisson's ratio	0.3
	Free space permittivity of air( $pF/\mu m$ )	$8.85 \times 10^{-6}$
	Coefficient of thermal expansion ( $1/K$ )	$2.3 \times 10^{-6}$
Device dimensions ( $\mu m$ )	Mirror	$100 \times 100$
	Suspension	$62 \times 4$
	Mirror and suspension thickness	2
	Electrode	$100 \times 100$

In conjunction with the mass-spring model, Ansys Multiphysics coupled-field finite element modeling package was used to solve for the coupled electrostatic/structural system response using the command macro ESSOLV. The stiffness calculated from the coupled-field finite element analysis model was approximately  $55.25 \text{ N/m}$ , and the stiffness using mass-spring system model resulted in  $66.141 \text{ N/m}$  for a 13 % error. The error could be due to meshing and modeling the suspension appropriately.

### 3.2 Kinematics of 3-DOF Plate

In this section we develop the kinematics of a 3-DOF flat plate. As shown in Fig. 9, the mirror at it's initial position have the same coordinates in the inertial  $I$  and the moving  $M$  coordinate frame. The mirror is free to rotate about the  $Z$  axis  $\theta$  degrees, rotate about the  $X$  axis  $\phi$  degrees, and translate  $y$  in the  $Y$  axis. The moving frame is attached to the to the plate.

The transformation matrix  $[T]$ , transforms the vector  $\vec{x}$  from the moving coordinate frame to the inertial coordinate frame vector  $\vec{X}$ , where  $\vec{X} = [T]\vec{x}$ . Transformation matrix is made of the rotational matrix  $[A]$  and the translational vector

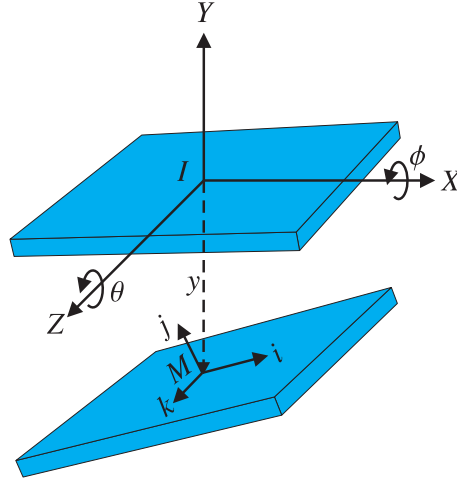


Figure 9: A flat plate with three degrees of freedom.

$\vec{r}$ , where  $[A] = [R_\theta][R_\phi]$ .

$$[T] = \begin{pmatrix} [A] & \vec{r} \\ 0 & 0 & 0 & 1 \end{pmatrix} \quad (3.16)$$

Multiplying the two rotational matrices,

$$[R_\theta] = \begin{pmatrix} \cos \theta & -\sin \theta & 0 \\ \sin \theta & \cos \theta & 0 \\ 0 & 0 & 1 \end{pmatrix}, [R_\phi] = \begin{pmatrix} 1 & 0 & 0 \\ 0 & \cos \theta & -\sin \theta \\ 0 & \sin \theta & \cos \theta \end{pmatrix} \quad (3.17)$$

Results in,

$$[T] = \begin{pmatrix} \cos \theta & -\sin \theta \cos \phi & \sin \theta \sin \phi & 0 \\ \sin \theta & \cos \theta \cos \phi & -\cos \theta \sin \phi & d \\ 0 & d \sin \phi & d \cos \phi & 0 \\ 0 & 0 & 0 & 1 \end{pmatrix} \quad (3.18)$$

This transformation  $[T]$  matrix defines the orientation and the translation of the 3-DOF plate with respect to the inertial frame.

Table 2: Table of stiffness values for various suspension designs

Suspension design	$k_y(N/m)$	$k_z(N/m)$
Simple beam	5.63	$2.04 \times 10^4$
Single serpentine	1.54	161.20
Double serpentine	0.99	80.87
Parallel beam	5.78	23.71
Tunable suspension	1.66	57.74

### 3.3 Suspension Modeling

Residual stress and stress gradient cause bowing of the mirror and reduces performance significantly. To compensate for this effect stiffness comparison between possible passive suspensions are made in this section. The suspensions are attached as seen in Fig. 8. All suspension were modeled by fixing at the anchor, and allowing 6-DOF at the point of the load. Using polysilicon properties from Table 1, stiffness in stress relief direction  $z$ , and in the actuation direction  $y$  are analyzed for a simple beam, single serpentine, double serpentine, parallel, and tuning suspension designs, results of modeling are shown in Fig. 10. Results from Table 2 show that the simple beam suspension have significantly higher stiffness in the direction of the residual stress force. Furthermore the parallel suspension have  $k_y$  value 2.67% within the simple beam suspension, but provide considerable compensation due to the significantly smaller  $k_y$  value. For the simple beam and the parallel beam, analytical model matched well with the FEA model, where  $k_y = 5.71 \text{ N/m}$  matching within 1.42 %. Additionally, stiffness of the parallel beam  $k_y$  was  $22.83 \text{ N/m}$ , matching within 3.71 %.



## 3.4 Modeling Performance Limits of a Fabry-Perot Filter

In this section we model common imperfections, such as composite misregistration, and unexpected perturbation as a result of thermal expansion. Using results described in Ch. 2, a relationship between mirror imperfections and effective finesse is developed. In particular, defects arising as a result of mask misregistration and thermal expansion are modeled. Results of modeling are projected to parallel deviations from a planar surface, and then used to solve for effective finesse Eq. (2.8) and the transmission profile, Eq. (2.11). Although, in a real system, all imperfections are present simultaneously, the model serve as vehicle to understanding performance limitations caused by common problems resulting from MEMS technology.

### 3.4.1 Misregistration

An electrostatically actuated micro-machined tunable Fabry-Perot interferometer includes suspensions for suspending the mirror above electrodes for actuation. Accumulative composite misregistration between mirror and electrode occurs during masking stages of surface micromachining or during wafer assembly. This leads to misalignment of electrodes causing mirror deviation from parallel as a result of uneven electrostatic pressure under the mirror during actuation (Fig. 11). Hence, modeling for a tunable-cavity Fabry-Perot filter with expected mask or wafer assembly misregistration was performed using properties from Table 1. Simulation was done by offsetting the electrodes from  $1\ \mu m$  to  $4\ \mu m$  along one of the plane axis, in increments of  $1\ \mu m$ . For each offset parameter, the mirror was actuated by applying  $0\ V$  to  $38\ V$ , causing vertical and angular mirror deflection due to uneven electrostatic pressure distribution. When  $0.5\ \mu m$  vertical deflection was reached

for different offset parameters, angular deflection of 2.5, 3.8, 6.1, and  $8.8 \times 10^{-3}$  degrees were calculated, that corresponded to 1  $\mu m$ , 2  $\mu m$ , 3  $\mu m$ , and 4  $\mu m$  electrode offsets. Fig. 12(a) is a plot of effective finesse as a function of reflectivity for misregistrations 1  $\mu m$  ( $A_1$ ), 2  $\mu m$  ( $A_2$ ), 3  $\mu m$  ( $A_3$ ), and 4  $\mu m$  ( $A_4$ ). All codes for Matlab and Ansys is in Appendix A and Appendix B.

Although the non-parallelism defect is not critical when reflectivity is between 85 % to 93 %, finesse dependence becomes much more pronounced as reflectivity increases, Fig. 12(a). For instance, effective finesse of an ideal FPF is 61 and 155 for reflectivity values of 95 % and 98 %, but with 4  $\mu m$  mask misregistration causing  $8.8 \times 10^{-3}$  degrees tilt ( $A_4$ ), the effective finesse reduces to 55 and 90, respectively. This indicates that defects are the limiting factor as reflectivity approaches 100 %. A complementing transmission profile for all misregistration at 98 % reflectivity is plotted in Fig. 12(b). As misregistration increases, fringe broadening effect becomes more apparent.

### 3.4.2 Thermal Expansion

Expected operational temperature range for Fabry-Perot filters is between  $-20^\circ C$  and  $80^\circ C$  (258.15  $K$  to 358.15  $K$ ). From thermal expansion modeling results, mirror vertical deflection of -15.6  $nm$ , -7.8  $nm$ , 0  $nm$ , 7.8  $nm$ , 15.6  $nm$ , and 23.3  $nm$  were calculated, corresponding to 258.15  $K$  ( $B_1$ ), 278.15  $K$  ( $B_2$ ), 298.15  $K$  ( $B_3$ ), 313.15  $K$  ( $B_4$ ), 333.15  $K$  ( $B_5$ ), and 358.15  $K$  ( $B_6$ ) atmospheric temperature, respectively. Similar to the non-parallel mirror case, cavity gap fluctuates with temperature, broadening bandwidth, and reducing finesse. Although temperature fluctuation is not a mirror defect, conceptually one can visualize the thermal expansion as an instantaneous plate deflection. Therefore, thermal expansion of the mirror can be represented as a non-parallel plate defect. Fig. 13(a) is a plot of effective finesse as a function of reflectivity for various thermal expansion cases.

Using reflectivity of 95 % and 98 % as in the previous example, 80  $K$  increase ( $B_6$ ) decreases effective finesse by approximately 16 % and 47 %, respectively. Fringe broadening effects caused by temperature fluctuations are plotted in Fig. 13(b). Initially at 98 % reflectivity, an ideal Fabry-Perot filter's ( $B_3$ ) bandwidth (full width half maximum) equals 13  $nm$ , at 358.15  $K$  ( $B_6$ ) fringe broadens to approximately 42  $nm$ . All codes for Matlab and Ansys is in Appendix A and Appendix B.

### 3.5 Conclusion

In this chapter the center deflection of the suspended Fabry-Perot mirror was modeled using a both mass-spring system and coupled-field FEA. Results from the coupled-field FEA and mass-spring model show that stiffness were within 13%. Stiffness of various suspensions were analyzed, and we concluded that a parallel beam suspension will have the same stiffness in the out of plane direction but will have significantly lower stiffness values to compensate for residual stress of the mirror. Coupled-field FEA was also implemented in junction with the results from Ch. 2 to characterize the performance limitations of an imperfect Fabry-Perot filter due to non-parallelism defects for both accumulative component misregistration and thermal expansion. In practice, multiple defects are present, and results from this section provide an insight to the sensitivity of passive micromachined tunable-cavity Fabry-Perot filters.

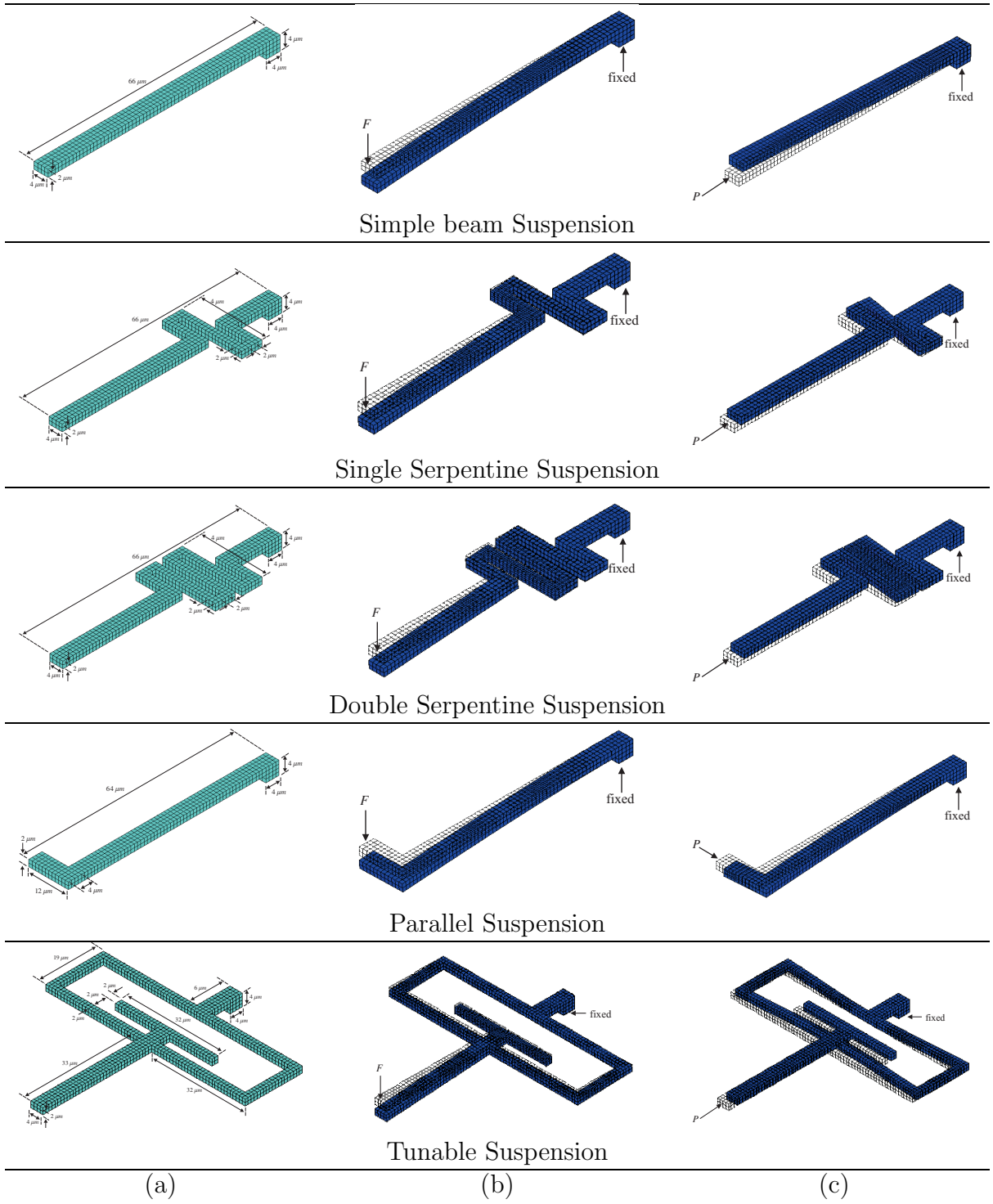


Figure 10: (a) Suspension design. (b) Force load in  $y$ . (c) Pressure load in  $z$ .

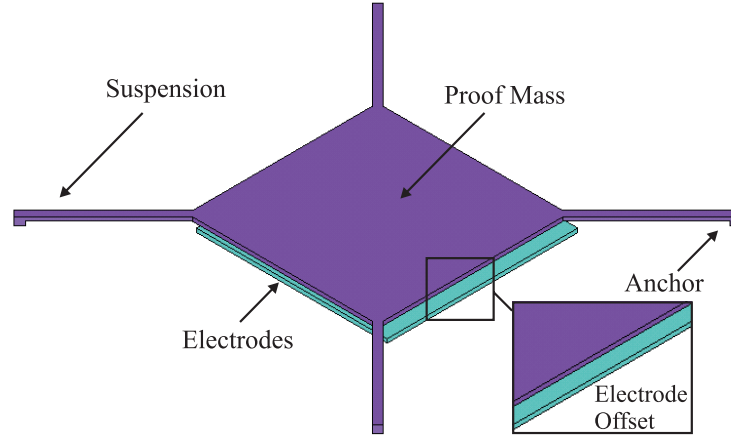


Figure 11: An example of mask misregistration during surface micromachining.

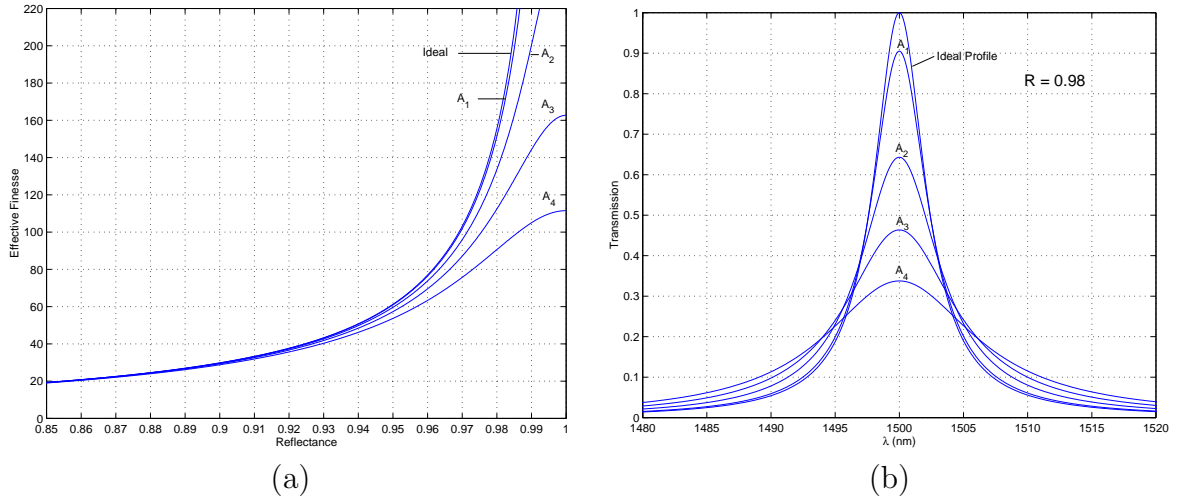


Figure 12: (a) A reduction in effective finesse as a result of even electrostatic pressure on the suspended mirror caused by component misregistration. (b) Fringe broadening effect as a result of even electrostatic pressure on the mirror caused by component misregistration.

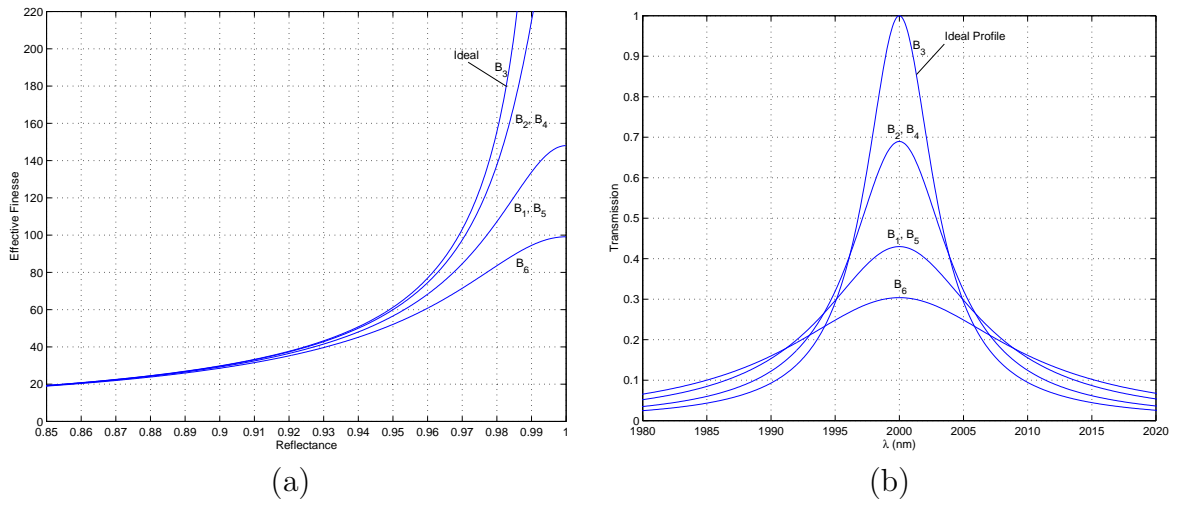


Figure 13: (a) A reduction in effective finesse caused by thermal expansion. (b) Fringe broadening effect as a result of thermal expansion.

# Chapter 4

## Fabry-Perot Filter Design

In this chapter a review of MUMPs surface micromachining process used for fabrication is presented, followed by the specific designs and a detail layout using L-Edit implemented in the Cronos MUMPs 39 run.

### 4.1 MUMPs Surface Micromachining Process

Multi-User MEMS Processes (MUMPs) is a three-layer polysilicon surface micromachining fabrication process with proof-of-concept through design rules available commercially for cost-effective development of MEMS devices. Starting with an n-type (100) wafers, a 600 nm blanket layer of low nitride (*Nitride*) is deposited followed by a blanket layer of 500 nm polysilicon (*Poly0*). *Poly0* it is coated with a layer of photoresist, and lithographically patterned by exposing it to UV through the first level mask (*Poly0*) and developed. Reactive ion etching (RIE) removes the unwanted polysilicon patterned by the photoresist mask, the remaining photoresist is stripped away. Then the first sacrificial 2.0  $\mu\text{m}$  layer of PSG (*Oxide1*) is deposited on the wafer. Again, by applying photoresist, etching, and stripping *Oxide1* is patterned using the same method. Then a blanket of 2.0  $\mu\text{m}$  layer of polysilicon (*Poly1*) is deposited, and steps are repeated until *Poly2* is reached, then metal layer is deposited. Specific structural patterns include dimples, holes, *Poly1 Poly2 via*, and anchors. Design rules for the MUMPs Design Handbook is available through Cronos' website (<http://www.memsrus.com/>). An example of a micromotor is shown in Fig. 14

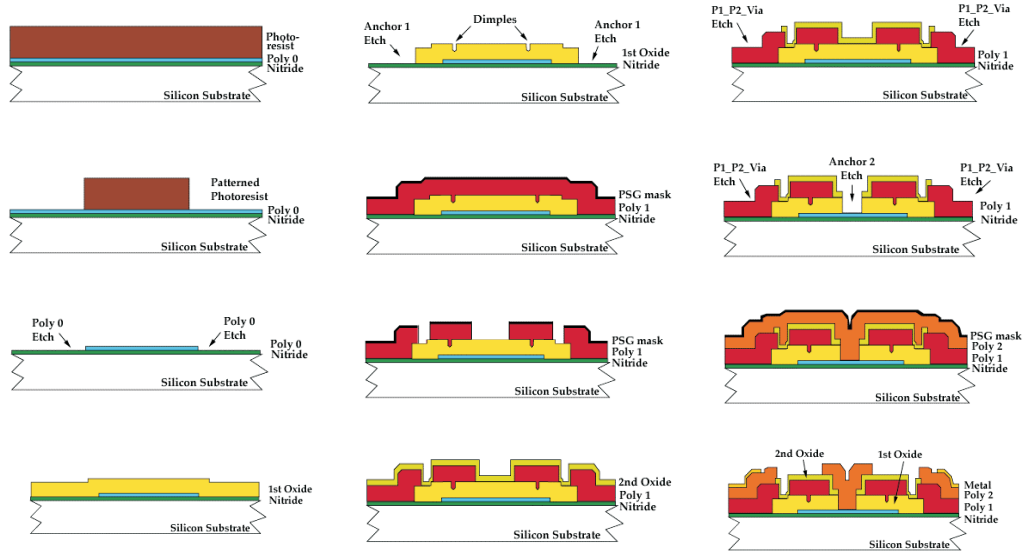


Figure 14: MUMPs technology uses a two polysilicon structural layer fabrication process.

## 4.2 Design of Fabry-Perot Interferometers using MUMPs Technology

Several mirror designs were implemented. The design variations were mirror with holes, mirror area, mirror layers, and various suspensions. Following MUMPs design rules, a  $100 \times 100 \mu m$  mirror required holes to provide an area for etching. Consequently, a smooth flat reflective surface desirable in Fabry-Perot interferometers were not achieved. Dispersion of light and electrostatic fringing fields make holes undesirable. Therefore, both designs were used in hopes that the mirrors without holes would still be fully released. Two different types of mirrors were designed, a cross sectional view is shown in Fig. 15. The mirror made of *Poly1 + Poly2 + Metal* forms a cavity gap of  $2 \mu m$ , whereas the *Poly2 + Metal* in formed on top of a ring of *Poly1* forming a cavity gap of  $2.75 \mu m$ , thus having a long range of actuation. Also, mirror area were increased by adding trapezoidal *Poly1* extension on each of the four sides to increase the mirror surface area, dimensions



of the extension were  $166\ \mu\text{m} \times 84\ \mu\text{m} \times 16\ \mu\text{m}$ .

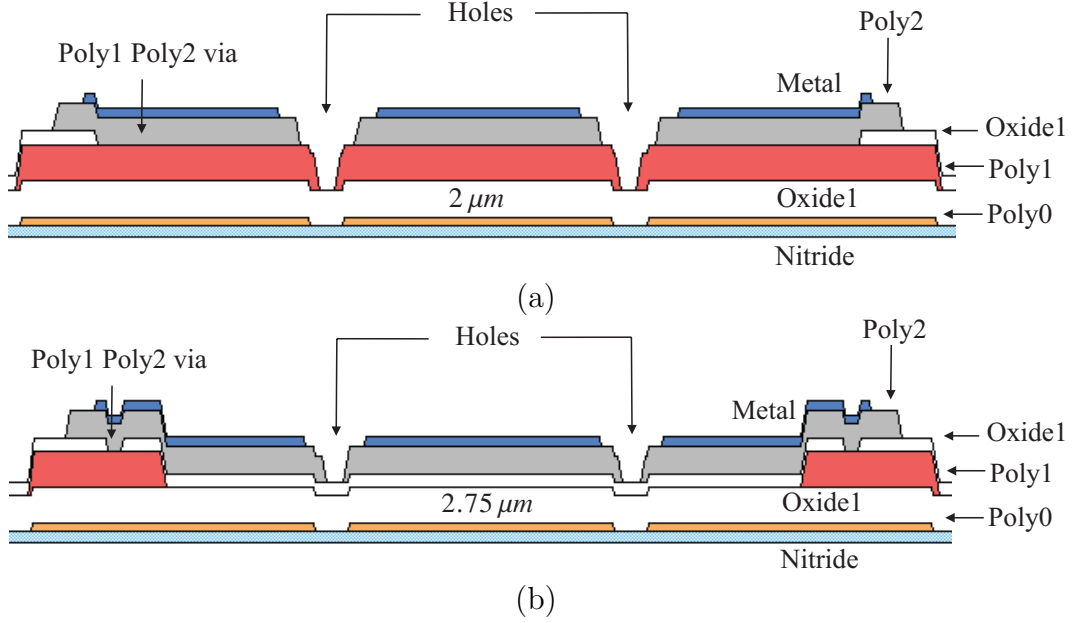


Figure 15: (a) *Poly1 + Poly2 + Metal* forming a 2  $\mu\text{m}$  gap. (b) *Poly2 + Metal* supported by ring of *Poly1* connected to the suspensions forming a 2.75  $\mu\text{m}$  gap.

In addition to several mirror designs, four different suspension designs were also included, Fig. 16. The single serpentine, double serpentine suspension, and tunable suspensions were attached diagonally on each corner suspending the mirror. The parallel suspensions were of the mirror. While all of the suspensions provide passive stress relief, tunable suspensions have capacitor plate built inside the outer ring to provide control over the stiffness and deflection. By actively controlling the suspension, mirror misalignment or independent control of individual suspension can be utilized to maintain mirror parallelism critical for maintaining high performance. Three dimensions for the serpentine suspension, three for tuning suspension, and four for the parallel suspension were incorporated to design variations. The various design variations and the overall layout scheme is described in detail in Appendix C. A layout using L-Edit of a single device is shown in Fig. 17.

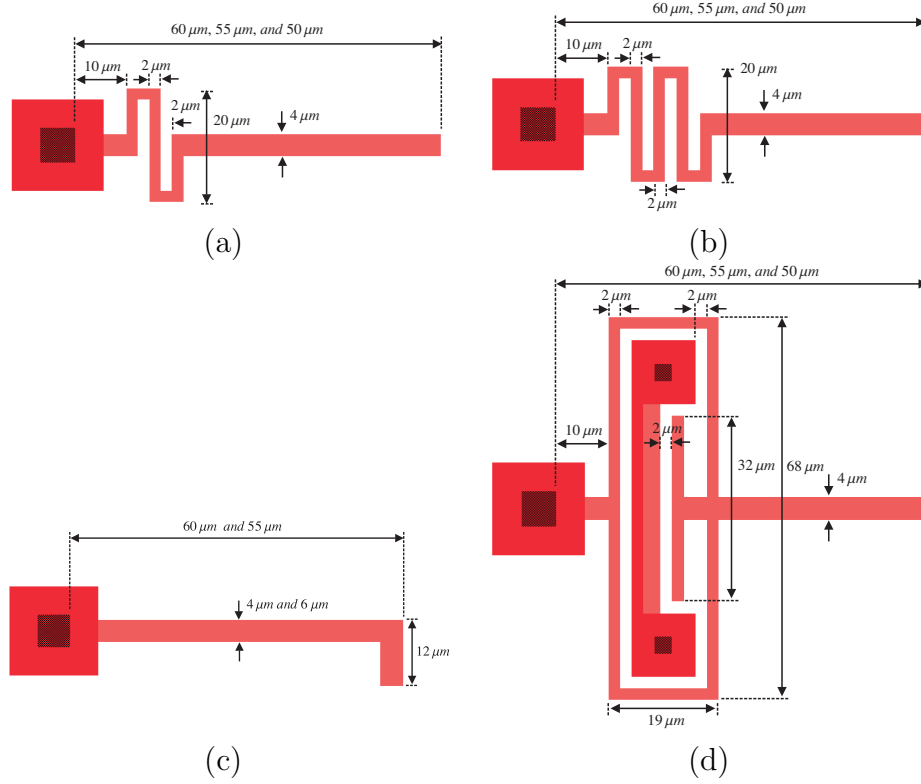


Figure 16: (a)Single serpentine passive suspension. (b)Double serpentine passive suspension. (c)Parallel passive suspension. (d)Tunable active suspension

### 4.3 Designs of an Experiment

An SEM photograph of fabricated devices from MUMPs run 39 are shown in Fig. 18.

An SEM photograph of an array of Fabry-Perot filters and a close-up of a single filter is shown in Fig. 19

### 4.4 Conclusion

In this chapter we describe fabrication process used to developed the prototype devices using MUMPS technology. This technology allows fast turnaround time for developing prototype device. Various designs and labeling methods were described

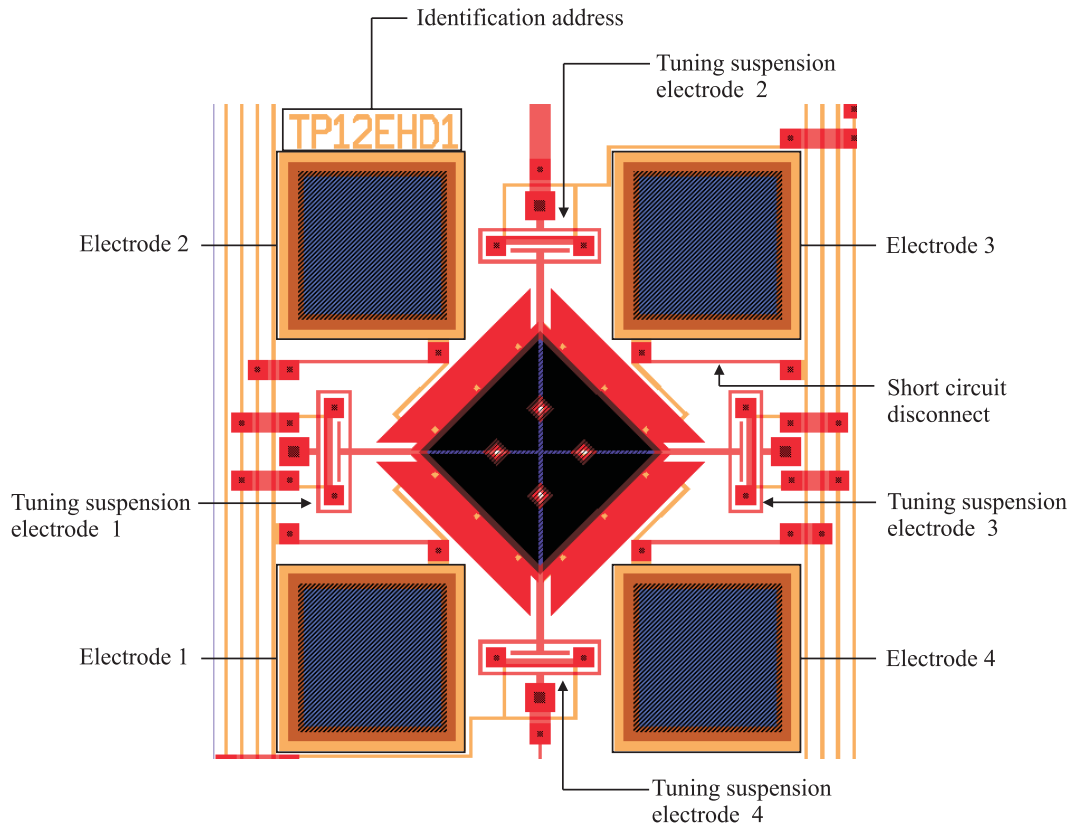


Figure 17: Identification tags for the Fabry-Perot design and electrodes for the mirror and tuning suspensions.

in this chapter, with detailed description of the layout scheme in Appendix ??.

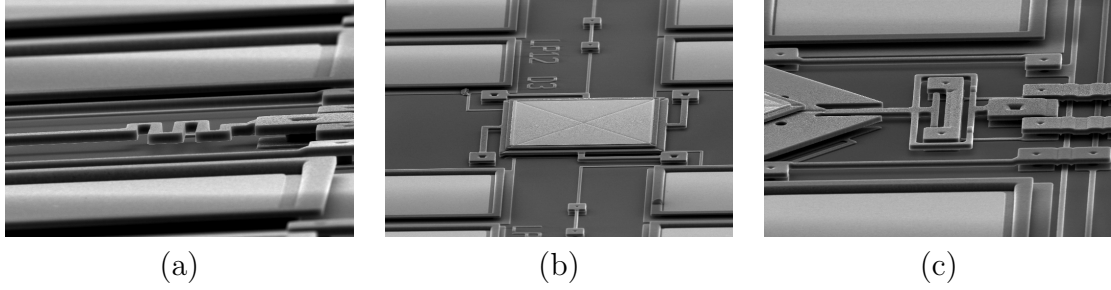


Figure 18: (a)SEM close-up of a double serpentine suspension. (b)SEM of a Fabry-Perot filter with parallel suspension. (c)SEM close-up of an active tune suspension.

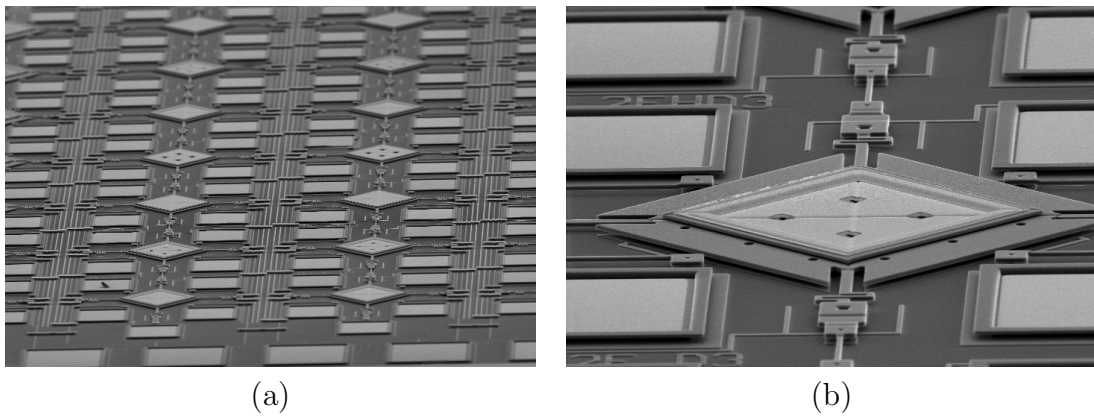


Figure 19: (a)SEM of an array of micromachined Fabry-Perot interferometers. (b)SEM of a micromachined Fabry-Perot interferometers with serpentine suspensions.

# Chapter 5

## Procedure for Testing

This section is a procedure for experimentally taking deflection measurements. Optical measurement is most desirable because it does not require contact. This can be done using a modified Michaelson interferometer [23], illustrated in Fig. 20. The light source (HeNe laser) is aligned by mirrors M1 and M2, and a beam splitter BS divides it into two orthogonal beams. Beam B1 used as the reference is reflected by M3 to BS. Meanwhile, beam B2 is focused on the microstructure and the reflection from the measured structured returns to the beam splitter, where it is recombines with the reference beam. This beam passes through a diverging lens so that only the fringe patten near the selected area is measured by the photodiode. Assuming the deflection  $\delta$  is small, the intensity  $I$  is linearly proportional to  $\delta$ ,

$$I(t) = I_1 + I_2 + \frac{1}{2}B \sin \left[ \frac{2\pi\delta(t)}{\lambda} \right] \quad (5.19)$$

where

$$B = 2\sqrt{I_1 I_2} \quad (5.20)$$

Another method for deflection measurement is by setting up a high reflective mirror parallel to the device, and sending a broadband signal, while measuring the intensity profile with a optical spectrum analyzer. Using principles discussed in Ch. 2, deflection measurements can be calculated based on the Fabry-Perot principle.

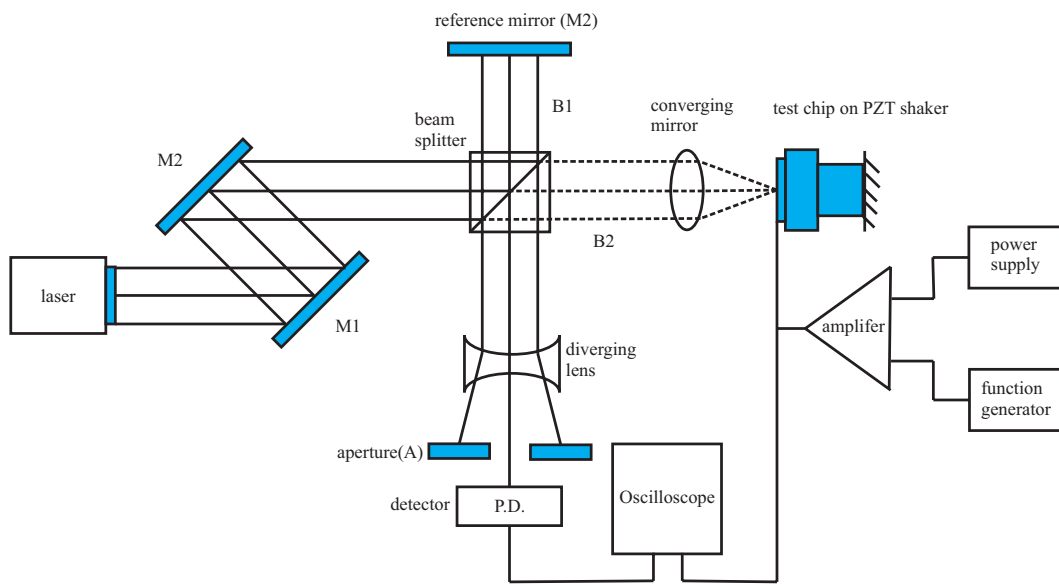


Figure 20: Modified Michelson interferometer for deflection measurement .

# Chapter 6

## Conclusion

The paper studied the potential for implementing a high performance tunable-cavity interferometer using MEMS technology. It was concluded, based on thermal expansion and component misregistration analysis, that a passive Fabry-Perot filter cannot achieve performance required for DWDM applications. For this application, in order to transmit 40-channels, finesse must be equal to approximately 1000, where spacing of 100  $GHz$  (0.8  $nm$ ) and bandwidth up to 10  $GHz$  (0.08  $nm$ ) are needed. By depositing gold or silver, reflective materials typically used in optical MEMS applications, 95 % reflectivity can be achieved. At this reflectivity, finesse for an ideal Fabry Perot filter is approximately 61. However, finesse is further aggravated by misregistration, resulting in mirror tilt on the order of 0.01 degrees, reducing effective finesse by as much as 10 % at 95 % mirror reflectivity. Using the same 40-channels example, reflectivity must be higher than 99.69 % to be useful for DWDM applications. Current MEMS technology does not satisfy these requirements. However, if MEMS technology is integrated with dielectric coating technology, where multiple dielectric coatings are applied, desirable reflection can be achieved. The use of dielectric coatings requires additional fabrication steps and introduces residual stress that induces mirror curvature. Furthermore, if the defect finesse is greater than the reflectivity finesse, there is no benefit in applying a high reflectivity coating. This tradeoff between development of new fabrication technology and potential for active compensation of imperfections will be the future focus of this research group.

## 6.1 Future Work

Future work will involve:

- Building infrastructure for testing.
- Integration of sensors to compensate for deviations of environmental conditions.
- Development of integrated MEMS technology suitable for micro-interferometers (i.e. integrating dielectric coatings).
- Setting up active feedback compensation for imperfections (i.e. non-parallelism), illustrated in Fig. 21.
- Develop packaging.

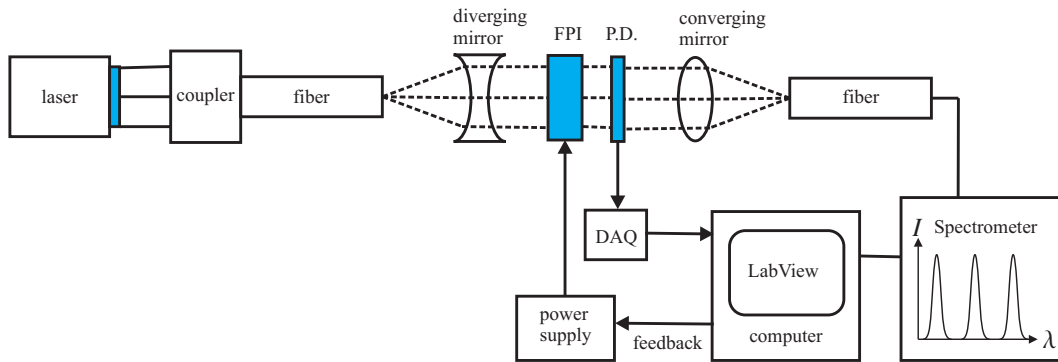


Figure 21: Future work will involve setting up a feedback system to increase performance. Fiber to fiber alignment device in conjunction with a collimating lens, laser, fiber, and a spectrometer can be used for measuring the transmitted intensity of micro Fabry-Perot interferometers. Using the quadrant detectors as feedback, we can analyze performance improvement from the optical spectrum analyzer.



# Bibliography

- [1] M. Christopher. Multipole light switch or multiplexer using rotator and interferometer. Patent Number: 5,949,580, September 1999.
- [2] R. Bayt M. Miller, M. Allen and K. Breuer. Design and testing of micromachined fabry-perot pressure sensor for aerodynamic applicatios. *38th AIAA Aerospace Sciences Meeting & Exhibit*, pages 1–13, January 2000.
- [3] Y. Yee. Pzt actuated micromirror for nano-tracking of laser beam for high-density optical data storage. *Proceedings IEEE Thirteenth Annual International Conference on Micro Electro Mechanical Systems*, pages 435–440, November 2000.
- [4] S. Kartalopoulos. *Introduction to DWDM Technology: Data in a Rainbow*. SPIE Optical Engineering Press, 2000.
- [5] J. Titus. DWDM communications rely on basic test techniques. Web: [http://www.tmworld.com/articles/2000/03\\_dwdm.htm](http://www.tmworld.com/articles/2000/03_dwdm.htm), March 2000.
- [6] J. Jerman and D. Clift. A miniature fabry-perot interferometer micromachined in silicon for use in optical fiber wdm systems. *International Solid-State Conference on Sensors and Actuators*, 29(2):472–475, 1991.
- [7] C. Palmer. *Diffraction Grating Handbook*. Richardson Grating Laboratory, fourth edition, 2000.
- [8] D. Clift J. Jerman and S. Mallinson. A miniature fabry-perot interferometer with a corrugated silicion diaphragm support. *Sensors and Actuators A (Physical)*, 29(2):140–144, November 1990.

- [9] S. Lee M. Wu L. Lin, J. Shen and A. Sergent. Tunable three-dimensional solid fabry-perot etalons fabricated by surface-micromachining. *IEEE Photonics Technology Letters*, 8(1):101–103, January 1996.
- [10] A. Vogt M. Tilsch C. Hebel F. Langenhan P. Meissner J. Peerings, A. Dehe and H. Hartnagel. Long resonator micromachined tunable gaas-alas fabry-perot filter. *IEEE Photonics Technology Letters*, 9(9):1235–1237, September 1997.
- [11] M. Azimi L. Maflah P. Tayebati, P. Wang and D. Vakhshoori. Microelectromechanical tunable filter with stable half symmetric cavity. *Electronics Letters*, 34(20):1967–1968, July 1998.
- [12] S. Tolansky. *Multiple-Beam interferometry of surface and films*. Dover Publications, Inc., 1970.
- [13] J. Vaughan. *The Fabry-Perot Interferometer (History, Theory, Practice and Applications)*. Adam Hilger, 1989.
- [14] W. Steel. *Multiple-Beam interferometry of surface and films*. Dover Publications, Inc., second edition, 1948.
- [15] S. Tolansky. *An Introduction to Interferometry*. John Wiley & Sons Inc., 1955.
- [16] H. Boukari E. Palik and R. Gammon. Experimental study of the effects of surface defects on the finesse and contrast of a fabry-perot interferometer. *Applied Optics*, 35(1):38–50, January 1996.
- [17] G. Sloggett. Fringe broadening in fabry-perot interferometers. *Applied Optics*, 23(14):2427–2432, July 1984.

- [18] Y. Min. Modeling, design, fabrication and measurement of a single layer polysilicon micromirror with initial curvature compensation. *Sensors and Actuators A (Physical)*, 78(1):7–17, November 1990.
- [19] C. Roychoudhuri and M. Hercher. Stable multipass fabry-perot interferometer: design and analysis. *Applied Optics*, 16(9):2514–2520, September 1977.
- [20] J. Ring P. Atherton, N. Reay and T. Hicks. Tunable fabry-perot filters. *Optical Engineering*, 20(6):806–814, November-December 1981.
- [21] J. McKay. Single and tandem fabry-perot etalons as solar background filters for lidar. *Applied Optics*, 38(27):5851–5857, September 1999.
- [22] W. Young. *Roark's Formulas for Stress & Strain*. McGraw-Hill Inc., sixth edition, 1989.
- [23] J. Jung-Yeul. Elimination of extra spring effects at the step-up anchor of surface-micromachined structure. *Journal of Microelectromechanical Systems*, 7(1):114–121, March 1998.

# Appendix A

## Matlab Codes

### A.1 intentsity.m

```
% This program plots the intensity profile (intensity.m)
m = linspace(1.5,2.5,10000)'; % Order number of interference

% Constants
d = 2e-6 ; % Cavity gap
R = .98 ; % Mirror reflectivity
T = .02 ; % Mirror transmittance
A = 1-(T+R) ; % Mirror absorption
theta = 0 ; % Incident beam angle

% Surface imperfections
del_p = 0 ; % Parallelism defect
del_s = 0 ; % Curvature defect
del_rms = 0 ; % Surface aperture following Gaussian distribution

% Solve for F_R, F_D, and F_E
F_R = pi*sqrt(R)/(1-R) ;
F_D = (2*d/2)/(4*del_s^2+22*del_rms^2+3*del_p^2)^.5 ; % (lambda = 2d/m m=2)
F_E = (F_R^-2+F_D^-2)^-.5 ;

% Solve for R_E
R_E = min(roots([F_E^2 -2*F_E^2-pi^2 F_E^2])) ;

% Airy function for an imperfect etalon
I_pk = (1-A/(1-R))^2*((1-R)/(1+R))*((1+R_E)/(1-R_E)) ;
T = I_pk*((1-R_E)^2/(1+R_E^2-2*R_E*cos(2*pi.*m))) ;

% Plot Intensity vs. wavelength
plot(2*d./m*10^9,T), hold on
```

### A.2 finesse.m

```
% This program calculates the intrumental finesse (finesse.m)

% Order number of interference
R = linspace(.8,.9999,1000)';

% Constants
d = 2e-6 ; % Cavity gap
R = .98 ; % Mirror reflectivity
T = .02 ; % Mirror transmittance
A = 1-(T+R) ; % Mirror absorption
theta = 0 ; % Incident beam angle

% Enter defects
del_p = 0 ; % Parallelism defect
del_s = 0 ; % Curvature defect
del_rms = 0 ; % Surface aperture following Gaussian distribution

% Solve for F_R, F_D, and F_E
F_R = pi.*sqrt(R)/(1-R) ;
F_D = (2*d)/(4*del_s^2+22*del_rms^2+3*del_p^2)^.5 ; % (lambda = 2d/m m=1)
F_E = (F_R^-2+F_D^-2)^-.5 ;

% Plot Transmittance function vs lambda
% plot(R,F_R), hold on % Delete % to plot F_R
plot(R,F_E), hold on % Plot F_E vs. reflectivity
```

# Appendix B

## Ansys Codes

### B.1 Coupled-Field Finite Element Analysis

#### B.1.1 electrostatic.txt

```

! Coupled-field electrostatic analysis

/ prep7
*SET, dx, 1                                ! misregistration
CSYS, 4
wpof, 100, 0, 0
et, 1, 122                                ! element type overlapping air
et, 2, 122                                ! element type mirror and beams
emunit, epzro, 8.854e-6                    ! units
mp, perx, 1, 1                             ! material prop
BLOCK, , 100, , 2, , 100,                 ! upper mirror
/VIEW, 1, 1, 1, 1
/ANG, 1
/REP, FAST
wpof, 98
BLOCK, , 4, , 2, , -66,                   ! creat suspension
wpof, 0, 0, -66
BLOCK, , 4, , -2, , 4,
wpof, 2, 0, 66
FLST, 2, 2, 6, ORDE, 2                    ! add volume and area
FITEM, 2, 2
FITEM, 2, -3
VADD, P51X
FLST, 2, 2, 5, ORDE, 2
FITEM, 2, 7
FITEM, 2, 19
AADD, P51X
FLST, 2, 2, 5, ORDE, 2
FITEM, 2, 21
FITEM, 2, 24
AADD, P51X
FLST, 2, 2, 5, ORDE, 2
FITEM, 2, 22
FITEM, 2, -23
AADD, P51X
wpstyle, 1, 0.1, -1, 1, 0.003, 0, 2, , 5 ! rotate and move suspension
wpro, , 90.000000,
wpstyle, 1, 0.1, -1, 1, 0.003, 1, 2, , 5
FLST, 3, 1, 6, ORDE, 1
FITEM, 3, 4
VGEN, , P51X, , , , 45, , , , 1
wpro, , -90.000000,
wpro, , 45.000000,
wpstyle, 1, 0.1, -1, 1, 0.003, 0, 2, , 5
FLST, 3, 1, 6, ORDE, 1
FITEM, 3, 4
VGEN, , P51X, , , -2, , , , 1
wpro, , -45.000000
wpof, dx, -2, 0! dx                        ! bottom mirror (electrode)
BLOCK, , -100, , -2, 100
wpof, -50-dx, 4, 50! - dx

FLST, 3, 1, 6, ORDE, 1                    ! volume suspension symmetry
FITEM, 3, 4
VSYMM, X, P51X, , , , 0, 0
FLST, 3, 2, 6, ORDE, 2
FITEM, 3, 3
FITEM, 3, -4
VSYMM, Z, P51X, , , , 0, 0
FLST, 2, 5, 6, ORDE, 3                    ! add volume and area

```

```

FITEM,2,1
FITEM,2,3
FITEM,2,-6
VADD,P51X
FLST,2,9,5,ORDE,9
FITEM,2,46
FITEM,2,-47
FITEM,2,49
FITEM,2,51
FITEM,2,57
FITEM,2,59
FITEM,2,61
FITEM,2,63
FITEM,2,66
AADD,P51X
FLST,2,9,5,ORDE,9
FITEM,2,45
FITEM,2,48
FITEM,2,50
FITEM,2,52
FITEM,2,58
FITEM,2,60
FITEM,2,62
FITEM,2,64
FITEM,2,-65
AADD,P51X
wpof,-150,2,-150                                !create air
BLOCK,,300,,,-10,,300,
FLST,2,3,6,ORDE,3
FITEM,2,1
FITEM,2,-2
FITEM,2,7
VOVLAP,P51X
VSEL,S,,,3                                !component air
CM,AIR,VOLU
ALLSEL,ALL
wpof,150,-2,150
VSEL,S,,,7
VPLOT
/DIST,1,0.729000,1
/REP,FAST
/DIST,1,0.729000,1
/REP,FAST
K,100,-50,,,                                !create keypoints
K,101,-50,-2,,
K,102,50,,,
K,103,50,-2,,
K,104,,,50,,
K,105,-2,50,
K,106,-50,,
K,107,-2,-50,
FLST,2,4,3                                !create area with keypoints
FITEM,2,101
FITEM,2,100
FITEM,2,102
FITEM,2,103
A,P51X
FLST,2,4,3
FITEM,2,105
FITEM,2,104
FITEM,2,106
FITEM,2,107
A,P51X
VPLOT

ALLSEL,ALL                                !subtract area from volume
FLST,3,2,5,ORDE,2
FITEM,3,20
FITEM,3,-21
VSBA,,7,P51X

FLST,2,4,6,ORDE,3                                !add volume
FITEM,2,1
FITEM,2,4
FITEM,2,-6
VADD,P51X
CM,_Y,VOLU
VSEL,,,7
CM,_Y1,VOLU
CMSEL,S,_Y
!*
CMSEL,S,_Y1
VATT,1,,2,0                                !assign attribute
CMSEL,S,_Y
CMDELE,_Y
CMDELE,_Y1
!*
CM,_Y,VOLU
VSEL,,,3
CM,_Y1,VOLU
CMSEL,S,_Y

```

```

!*
CMSEL,S,_Y1
VATT,1,,1,0
CMSEL,S,_Y
CMDELE,_Y
CMDELE,_Y1
!*
ESIZE,10,0,!mesh air
MSHAPE,1,3D
MSHKEY,0
!*
CM,_Y,VOLU
VSEL,,,3
CM,_Y1,VOLU
CHKMSH,'VOLU'
CMSEL,S,_Y
!*
VMESH,_Y1
!*
CMDELE,_Y
CMDELE,_Y1
CMDELE,_Y2
!*
ESIZE,5,0,!mesh mirror and beams
CM,_Y,VOLU
VSEL,,,7
CM,_Y1,VOLU
CHKMSH,'VOLU'
CMSEL,S,_Y
!*
VMESH,_Y1
!*
CMDELE,_Y
CMDELE,_Y1
CMDELE,_Y2

! Add boundry conditions , and solve
voltage=38!set voltage
FINISH
/SOLU!apply voltage and ground
FLST,2,4,5,ORDE,4
FITEM,2,37
FITEM,2,47
FITEM,2,52
FITEM,2,60
DA,P51X,VOLT,,
FLST,2,1,5,ORDE,1
FITEM,2,17
DA,P51X,VOLT,voltage,!apply voltage on electrodes
FINISH
/PREP7
et,2,0
PHYSICS,WRITE,elec,,,
PHYSICS,CLEAR
et,2,95
et,1,0
!*
UIMP,1,EX,,1.7e5,!young's modulus of polysilicon
UIMP,1,NUXY,,.3,!poissons ratio of polysilicon
UIMP,1,ALPX,,,
UIMP,1,REFT,,,
UIMP,1,MU,,,
UIMP,1,DAMP,,,
UIMP,1,DENS,,2.33e-15,!density of polysilicon
UIMP,1,KXX,,,
UIMP,1,C,,,
UIMP,1,ENTH,,,
UIMP,1,HF,,,
UIMP,1,EMIS,,,
UIMP,1,QRATE,,,
UIMP,1,VISC,,,
UIMP,1,SONC,,,
UIMP,1,MURX,,,
UIMP,1,MGXX,,,
UIMP,1,RSVX,,,
UIMP,1,PERX,,,
!*
FINISH
/SOLU
FLST,2,4,5,ORDE,4!anchor beams
FITEM,2,15
FITEM,2,25
FITEM,2,33
FITEM,2,41
!*
/GO
DA,P51X,ALL,
FINISH
/PREP7
PHYSICS,WRITE,struct,,,
!*

```

```

!*
ESSOLV, 'elec', 'struct', 3, 0, 'AIR', ' ', ' ', 0.1E-01, 0.1E-01, 100
/PREP7
PHYSICS, READ, struct
FINISH
/POST1
SET, LAST

FLST, 5, 3, 1, ORDE, 3           !select node and print all dofs
FITEM, 5, 10691
FITEM, 5, 10681                 !center node
FITEM, 5, 10831
NSEL, S, , , P51X

AVPRIN, 0, 0,
!*
PRNSOL, DOF,

```

## B.1.2 thermal.txt

```

! Coupled-field thermal expansion model

/prep7
*SET, dx, 0                     ! misregistration
CSYS, 4
wpof, 100, 0, 0
et, 2, 95                       ! element type mirror and beams
emunit, epzro, 8.854e-6        ! units
mp, perx, 1, 1                 ! material prop
BLOCK, , 100, , 2, , 100,      ! upper mirror
/VIEW, 1, 1, 1, 1
/ANG, 1
/REP, FAST
wpof, 98
BLOCK, , 4, , 2, , -66,        ! creat suspension
wpof, 0, 0, -66
BLOCK, , 4, , -2, , 4,
wpof, 2, 0, 66
FLST, 2, 2, 6, ORDE, 2        ! add volume and area
FITEM, 2, 2
FITEM, 2, -3
VADD, P51X
FLST, 2, 2, 5, ORDE, 2
FITEM, 2, 7
FITEM, 2, 19
AADD, P51X
FLST, 2, 2, 5, ORDE, 2
FITEM, 2, 21
FITEM, 2, 24
AADD, P51X
FLST, 2, 2, 5, ORDE, 2
FITEM, 2, 22
FITEM, 2, -23
AADD, P51X
wpstyle, 1, 0.1, -1, 1, 0.003, 0, 2, , 5 ! rotate and move suspension
wpro, , 90.000000,
wpstyle, 1, 0.1, -1, 1, 0.003, 1, 2, , 5
FLST, 3, 1, 6, ORDE, 1
FITEM, 3, 4
VGEN, , P51X, , , , 45, , , 1
wpro, , -90.000000,
wpro, , 45.000000,
wpstyle, 1, 0.1, -1, 1, 0.003, 0, 2, , 5
FLST, 3, 1, 6, ORDE, 1
FITEM, 3, 4
VGEN, , P51X, , , -2, , , , 1
wpro, , -45.000000
wpof, dx, -2, 0! dx           ! bottom mirror (electrode)
BLOCK, , -100, , -2, 100
wpof, -50-dx, 4, 50!-dx
FLST, 3, 1, 6, ORDE, 1        ! volume suspension symmetry
FITEM, 3, 4
VSYMM, X, P51X, , , , 0, 0
FLST, 3, 2, 6, ORDE, 2
FITEM, 3, 3
FITEM, 3, -4
VSYMM, Z, P51X, , , , 0, 0
FLST, 2, 5, 6, ORDE, 3        ! add volume and area
FITEM, 2, 1
FITEM, 2, 3
FITEM, 2, -6
VADD, P51X
FLST, 2, 9, 5, ORDE, 9
FITEM, 2, 46
FITEM, 2, -47
FITEM, 2, 49
FITEM, 2, 51

```



```

FITEM,2,57
FITEM,2,59
FITEM,2,61
FITEM,2,63
FITEM,2,66
AADD,P51X
FLST,2,9,5,ORDE,9
FITEM,2,45
FITEM,2,48
FITEM,2,50
FITEM,2,52
FITEM,2,58
FITEM,2,60
FITEM,2,62
FITEM,2,64
FITEM,2,-65
AADD,P51X
wpof,-150,2,-150      !create air
BLOCK,,300,,,-10,,300,
FLST,2,3,6,ORDE,3
FITEM,2,1
FITEM,2,-2
FITEM,2,7
VOVLAP,P51X
VSEL,S,,,3            !component air
CM,AIR,VOLU
ALLSEL,ALL
wpof,150,-2,150
VSEL,S,,,7
VPLOT
/DIST,1,0.729000,1
/REP,FAST
/DIST,1,0.729000,1
/REP,FAST
K,100,-50,,,          !create keypoints
K,101,-50,-2,,
K,102,50,,,
K,103,50,-2,,
K,104,,,50,
K,105,,,-2,50,
K,106,,,50,
K,107,,,-2,-50,
FLST,2,4,3            !create area with keypoints
FITEM,2,101
FITEM,2,100
FITEM,2,102
FITEM,2,103
A,P51X
FLST,2,4,3
FITEM,2,105
FITEM,2,104
FITEM,2,106
FITEM,2,107
A,P51X
VPLOT
ALLSEL,ALL            !subtract area from volume
FLST,3,2,5,ORDE,2
FITEM,3,20
FITEM,3,-21
VSBA,,7,P51X
FLST,2,4,6,ORDE,3     !add volume
FITEM,2,1
FITEM,2,4
FITEM,2,-6
VADD,P51X
CM,_Y,VOLU
VSEL,,,7
CM,_Y1,VOLU
CMSEL,S,_Y
!*
VDELE,,3,,1
VATT,,1,,2,0
VDELE,,2,,1
CM,_Y,VOLU
VSEL,,,7
CM,_Y1,VOLU
CMSEL,S,_Y
!*
CMSEL,S,_Y1
VATT,,1,,2,0
CMSEL,S,_Y
CMDELE,_Y
CMDELE,_Y1
!*
!*
UIMP,1,EX,,1.7e5,      !young modulus of polysilicon
UIMP,1,NUXY,,0.22,     !poissons ratio of polysilicon
UIMP,1,ALPX,,2.3e-6,   !thermal expansion of polysilicon
UIMP,1,REFT,,0,        !reference temperature
UIMP,1,MU,,

```

```

UIMP,1,DAMP, , , ,
UIMP,1,DENS, , , ,
UIMP,1,KXX, , , ,
UIMP,1,C, , , ,
UIMP,1,ENTH, , , ,
UIMP,1,HF, , , ,
UIMP,1,EMIS, , , ,
UIMP,1,QRATE, , , ,
UIMP,1,VISC, , , ,
UIMP,1,SONC, , , ,
UIMP,1,MURX, , , ,
UIMP,1,MGXX, , , ,
UIMP,1,RSVX, , , ,
UIMP,1,PERX, , , 1,      !permittivity of air
!*
ESIZE,5,0,
MSHAPE,1,3 D
MSHKEY,0
!*
CM,_Y,VOLU
VSEL, , , , 7
CM,_Y1,VOLU
CHKMSH,'VOLU'
CMSEL,S,_Y
!*
VMESH,_Y1
!*
CMDELE,_Y
CMDELE,_Y1
CMDELE,_Y2
!*
FINISH
/SOLU
/USER, 1
/VIEW, 1, 0.113205234008, 0.439647988744, 0.891007419153
/ANG, 1, -12.2051073400
/REPLO
FLST,2,4,5,ORDE,4
FITEM,2,15
FITEM,2,25
FITEM,2,33
FITEM,2,41
!*
/GO
DA,P51X,ALL,      !apply bc on achors
FLST,2,1,6,ORDE,1
FITEM,2,7
!*
BFV,P51X,TEMP,20      !load step 1: surface temperature condition
LSWRITE,1,
FLST,2,1,6,ORDE,1
FITEM,2,7
!*
BFV,P51X,TEMP,40      !load step 2: surface temperature condition
LSWRITE,2,
FLST,2,1,6,ORDE,1
FITEM,2,7
!*
BFV,P51X,TEMP,60      !load step 3: surface temperature condition
LSWRITE,3,
FLST,2,1,6,ORDE,1
FITEM,2,7
!*
BFV,P51X,TEMP,80      !load step 4: surface temperature condition
LSWRITE,4,
FLST,2,1,6,ORDE,1
FITEM,2,7
!*
BFV,P51X,TEMP,100     !load step 5: surface temperature condition
LSWRITE,5,
LSSOLVE,1,5,1,      !solve loadsteps

```

## B.2 Stiffness Analysis of Suspension Designs

### B.2.1 beam.txt

```

!Single serpentine suspension stiffness calculation
/PREP7
ET,1,SOLID95      !element type
UIMP,1,EX, , , 1.7 e5,      !young's modulus of polysilicon

```

```

wpof,100,0,0

BLOCK,2,-2,-1,1,-42,      ! create solid model
/VIEW, 1,1,1,1
/ANG, 1
/REP,FAST
VPLOT
wpof,,,-42
BLOCK,2,-10,-1,1,-2,
wpof,-10,-2
BLOCK,2,-1,1,-2,
wpof,,,-2
BLOCK,20,-1,1,-2,
wpof,20,-2
BLOCK,-2,-1,1,-2,
wpof,,,-2
BLOCK,-12,-1,1,-2,
wpof,-12,-2
BLOCK,4,-1,1,-14,
wpof,0,-1,-14
BLOCK,4,0,-2,,4,
wpof,2,1,66

FLST,2,8,6,ORDE,2          ! select and glue volumes
FITEM,2,1
FITEM,2,-8
VGLUE,P51X
ESIZE,1,0,                  ! set global mesh for 1
FLST,5,8,6,ORDE,3          ! select and hex mesh
FITEM,5,1
FITEM,5,9
FITEM,5,-15
CM,_Y,VOLU
VSEL,, , ,P51X
CM,_Y1,VOLU
CHKMSH,'VOLU'
CMSEL,S,_Y
!*
VSWEEP,_Y1
!*
CMDELE,_Y
CMDELE,_Y1
CMDELE,_Y2

FINISH                      ! bc 1
/SOLU
FLST,2,1,5,ORDE,1
FITEM,2,2
/GO
!*
SFA,P51X,1,PRES,10/8        ! select area and apply 10/8 N/m^2 at tip in z direction
FLST,2,1,5,ORDE,1
FITEM,2,45
!*
/GO
DA,P51X,ALL,                ! apply 0 dof at anchor
/STATUS,SOLU
SOLVE                      ! solve for solution

/eof
FINISH                      ! bc 2
/SOLU
FLST,2,1,5,ORDE,1
FITEM,2,45
!*
/GO
DA,P51X,ALL,                ! apply 0 dof at anchor
/STATUS,SOLU
SOLVE                      ! solve for solution

/STATUS,SOLU
SOLVE
F,P51X,FY,-10
/STATUS,SOLU
SOLVE

```

## B.2.2 single.txt

```

! Single serpentine suspension stiffness calculation

/PREP7

ET,1,SOLID95                ! element type
UIMP,1,EX, , ,1.7 e5,      ! young's modulus of polysilicon
wpof,100,0,0

BLOCK,2,-2,-1,1,-42,      ! create solid model
/VIEW, 1,1,1,1

```

```

/ANG, 1
/REP, FAST
VPLOT
wpof, , , -42
BLOCK, 2, -10, -1, 1, , -2,
wpof, -10, , -2
BLOCK, 2, , -1, 1, , -2,
wpof, , , -2
BLOCK, 20, , -1, 1, , -2,
wpof, 20, , -2
BLOCK, -2, , -1, 1, , -2,
wpof, , , -2
BLOCK, -12, , -1, 1, , -2,
wpof, -12, , -2
BLOCK, 4, , -1, 1, , -14,
wpof, 0, -1, -14
BLOCK, 4, 0, -2, , , 4,
wpof, 2, 1, 66

FLST, 2, 8, 6, ORDE, 2      !select and glue volumes
FITEM, 2, 1
FITEM, 2, -8
VGLUE, P51X
ESIZE, 1, 0,
FLST, 5, 8, 6, ORDE, 3      !set global mesh for 1
                                !select and hex mesh
FITEM, 5, 1
FITEM, 5, 9
FITEM, 5, -15
CM, _Y, VOLU
VSEL, , , , P51X
CM, _Y1, VOLU
CHKMSH, 'VOLU'
CMSEL, S, _Y
!*
VSWEEP, _Y1
!*
CMDELE, _Y
CMDELE, _Y1
CMDELE, _Y2

FINISH                      !bc 1
/SOLU
FLST, 2, 1, 5, ORDE, 1
FITEM, 2, 2
/GO
!*
SFA, P51X, 1, PRES, 10/8    !select area and apply 10/8 N/m^2 at tip in z direction
FLST, 2, 1, 5, ORDE, 1
FITEM, 2, 45
!*
/GO
DA, P51X, ALL,              !apply 0 dof at anchor
/STATUS, SOLU
SOLVE                      !solve for solution

/eof
FINISH                      !bc 2
/SOLU
FLST, 2, 1, 5, ORDE, 1
FITEM, 2, 45
!*
/GO
DA, P51X, ALL,
FLST, 2, 1, 1, ORDE, 1      !select and apply -10 N at tip
FITEM, 2, 621
!*
/GO
F, P51X, FY, -10
/STATUS, SOLU
SOLVE                      !solve

```

## B.2.3 double.txt

```

!Double serpentine suspension stiffness calculation

/PREP7

ET, 1, SOLID95              !element type
UIMP, 1, EX, , , 1.7 e5,    !young's modulus of polysilicon
wpof, 100, 0, 0

BLOCK, -2, 2, -1, 1, , -34, !build solid model
/VIEW, 1, 1, 1, 1
/ANG, 1
/REP, FAST
VPLOT
wpof, , , -34

```

```

BLOCK,2,-10,-1,1,-2,
wpof,-10,-2
BLOCK,2,-1,1,-2,
wpof,-2
BLOCK,20,-1,1,-2,
wpof,20,-2
BLOCK,-2,-1,1,-2,
wpof,-2
BLOCK,-20,-1,1,-2,
wpof,-20,-1,-2
BLOCK,2,0,0,2,-2,,
wpof,-2
BLOCK,20,0,2,-2,,
wpof,20,-2
BLOCK,-2,0,2,-2,,
wpof,-2
BLOCK,-12,0,2,-2,,
wpof,-12,-2
BLOCK,4,0,2,-14,,
wpof,-14
BLOCK,4,-2,,,4,
wpof,2,1,66

FLST,2,12,6,ORDE,2      !select and vglue
FITEM,2,1
FITEM,2,-12
VGLUE,P51X
ESIZE,1,0,              !global size mesh 1
FLST,5,12,6,ORDE,3      !select and sweep mesh
FITEM,5,1
FITEM,5,13
FITEM,5,-23
CM,_Y,VOLU
VSEL,,,P51X
CM,_Y1,VOLU
CHKMSH,'VOLU'
CMSEL,S,_Y
!*
VSWEEP,_Y1
!*
CMDELE,_Y
CMDELE,_Y1
CMDELE,_Y2
!*

FINISH                  !boundry conditions 1
/SOLU
FLST,2,1,5,ORDE,1      !select and apply 0 dof on anchor
FITEM,2,69
!*
/GO
DA,P51X,ALL,
FLST,2,1,1,ORDE,1      !select and apply force -10 N on tip in y direction
FITEM,2,713
!*
/GO
F,P51X,FY,-10
/STATUS,SOLU           !solve
SOLVE

/eof                    !end of file
FINISH                  !boundry conditions 2
/SOLU
FLST,2,1,5,ORDE,1      !select and 0 dof at anchor
FITEM,2,69
!*
/GO
DA,P51X,ALL,
FLST,2,1,5,ORDE,1      !select and apply pressure at tip 10/8 N/m^2 in z direction
FITEM,2,2
/GO
!*
SFA,P51X,1,PRES,10/8    !solve
/STATUS,SOLU
SOLVE

```

## B.2.4 parallel.txt

```

!Parallel serpentine suspension stiffness calculation

/PREP7

ET,1,SOLID95            !element type
UIMP,1,EX,,1.7e5,       !young's modulus of polysilicon
wpof,100,0,0

block,-12,,2,-4,,      !solid model

```

```

/VIEW, 1, 1, 1, 1
/ANG, 1
/REP, FAST
wpof, , -4
block, -4, , , 2, -60
wpof, , -60
block, -4, , , -2, , 4,
FLST, 2, 3, 6, ORDE, 2      !select and vglue
FITEM, 2, 1
FITEM, 2, -3
VGLUE, P51X
ESIZE, 1, 0,
FLST, 5, 3, 6, ORDE, 2      !select and mesh sweep mesh with global mesh=1
FITEM, 5, 4
FITEM, 5, -6
CM, _Y, VOLU
VSEL, , , , P51X
CM, _Y1, VOLU
CHKMSH, 'VOLU'
CMSEL, S, _Y
!*
VSWEEP, _Y1
!*
CMDELE, _Y
CMDELE, _Y1
CMDELE, _Y2
!*
FINISH                      !boundry conditions 1
/SOLU
FLST, 2, 1, 5, ORDE, 1      !select anchor 0 dof
FITEM, 2, 15
!*
/GO
DA, P51X, ALL,
WPSTYLE, , , , , , 0
FLST, 2, 1, 1, ORDE, 1      !select and apply force at tip
FITEM, 2, 2505
!*
/GO
F, P51X, FY, -10
/STATUS, SOLU
SOLVE

/eof
FINISH                      !boundry conditions 2
/SOLU
FLST, 2, 1, 5, ORDE, 1      !select and 0 dof on anchor
FITEM, 2, 15
!*
/GO
DA, P51X, ALL,
FLST, 2, 1, 5, ORDE, 1      !select and apply pressure
FITEM, 2, 5
/GO
!*
SFA, P51X, 1, PRES, 10/8    !solve
/STATUS, SOLU
SOLVE

```

## B.2.5 tune.txt

```

!Tunable suspension stiffness calculation

/prep7

CSYS, 4
wpof, 100, 0, 0

ET, 1, SOLID95              !element type
UIMP, 1, EX, , , 1.7 e5,    !young's modulus of polysilicon

/VIEW, 1, 1, 1, 1
/ANG, 1
/REP, FAST

BLOCK, , 4, , 2, , -36,      !creat suspension
wpof, 2
wpof, 0, 0, -36
BLOCK, , 2, , 2, , -8,
wpof, 0, 0, -8
BLOCK, , 16, , 2, , 2,
wpof, 0, 0, 8
BLOCK, , 33, , 2, , -2,
wpof, 33
BLOCK, , -2, , 2, , -19,
wpof, 0, 0, -19
BLOCK, , -33, , 2, , 2,

```

```

wpof,-33
wpof,0,0,4
BLOCK,,29,,2,,5,
wpof,29
BLOCK,,-11,,2,,11,
wpof,-29,0,-4
BLOCK,,2,,2,,-11,
wpof,0,0,-11
BLOCK,,2,,-2,,4,
wpof,0,0,66
CSYS,4
FLST,3,9,6,ORDE,2
FITEM,3,3
FITEM,3,-11
VSMM,X,P51X,, , ,0,0
FLST,3,1,6,ORDE,1
FITEM,3,2
VSMM,X,P51X,, , ,0,0

FLST,2,19,6,ORDE,2      !pick volume to overlap
FITEM,2,1
FITEM,2,-19
VOVLAP,P51X
FLST,2,23,6,ORDE,6      !pick volume to glue
FITEM,2,20
FITEM,2,-23
FITEM,2,28
FITEM,2,-31
FITEM,2,34
FITEM,2,-48
VGLUE,P51X
FLST,2,6,6,ORDE,4
FITEM,2,24
FITEM,2,-27
FITEM,2,32
FITEM,2,-33
VDELE,P51X,, ,1        !pick electrode and delete
ESIZE,1,0,
FLST,5,23,6,ORDE,6
FITEM,5,20
FITEM,5,-23
FITEM,5,28
FITEM,5,-31
FITEM,5,34
FITEM,5,-48
CM,_Y,VOLU
VSEL,, , ,P51X
CM,_Y1,VOLU
CHKMSH,'VOLU'
CMSEL,S,_Y
!*
VSWEEP,_Y1
!*
CMDELE,_Y
CMDELE,_Y1
CMDELE,_Y2

FINISH                  !boundry condition 1
/SOLU
FLST,2,2,5,ORDE,2
FITEM,2,57
FITEM,2,210
!*
/GO                      !apply 0 dof on anchor
DA,P51X,ALL,
FLST,2,1,1,ORDE,1
FITEM,2,2031
!*
/GO
F,P51X,FY,-10           !-10 N force on tip of cantilevel
/STATUS,SOLU
SOLVE                   !solve for solution

/eof                     !end of file
FINISH                  !boundry condition 2
/SOLU
FLST,2,2,5,ORDE,2
FITEM,2,57
FITEM,2,210
!*
/GO
DA,P51X,ALL,           !apply 0 dof on anchor
FLST,2,1,5,ORDE,1
FITEM,2,2
/GO
!*
SFA,P51X,1,PRES,10/8    !apply pressure 10/8^2 N/m^2 force
/STATUS,SOLU
SOLVE                   !solve

```

# Appendix C

## L-Edit Layout

### C.1 Labeling

As a result of the many mirror and suspension parameters, an identification addressing systems was developed and printed on the layout next to each design, Fig 22. The first column represents the suspension type. The second column represents the mirror layers. The third and fourth column represent whether the mirror has extensions and holes, respectively. The final column is for the dimensions of the suspension. For the serpentine and the tuning suspensions, D1, D2, and D3 have effective beam lengths of  $60\ \mu m$ ,  $55\ \mu m$ , and  $50\ \mu m$ , respectively. For the parallel suspension, D1 equals  $60\ \mu m$  length and  $4\ \mu m$  width, D2 equals  $60\ \mu m$  length and  $6\ \mu m$  width, D3 equals  $55\ \mu m$  length and  $4\ \mu m$  width, and D4 equals  $55\ \mu m$  length and  $6\ \mu m$  width. For example Fig.22 is a tunable suspension, *Poly1 + Poly2 + Metal* layer mirror, mirror extension, holes, and suspension with a  $60\ \mu m$  length. Layout of all the designs are shown in Fig. 23, and corresponds to the identification addresses in Table. C.1 .

A close up of a one design within the array of the layout is shown in Fig. 17. The identification tag is placed directly on top of electrode two. The mirror electrodes and tuning suspension electrodes are marked accordingly. Also to prevent short circuits, a *Poly1* bridge was made for disconnecting it from other devices which shared the same bonding pad. The letters are assigned to each column, See Fig. 23. Since the outer bonding pads were used for wire bonding and were limited,



individual column shared the electrodes. With the exception of the electrode for the suspension tuning and ground, the set of four electrodes under the suspended mirror shared the outer bonding pads for each column. Next to each outer bonding pad was a coding scheme for identify the corresponding electrodes, Fig. 17.

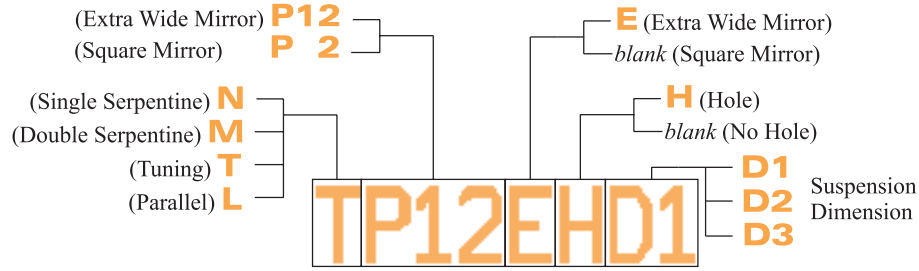


Figure 22: Reading the identification address.

Table 3: Design address corresponding to Fig. 23.

A	B	C	D	E	F	AA	BB	CC	DD
TP12EHD1	TP12EHD2	TP12EHD3	TP12HD1	TP12HD2	TP12HD3				
TP12ED1	TP12ED2	TP12ED3	TP12D1	TP12D2	TP12D3				
TP2EHD1	TP2EHD2	TP2EHD3	TP2HD1	TP2HD2	TP2HD3				
TP2ED1	TP2ED2	TP2ED3	TP2D1	TP2D2	TP2D3				
NP12EHD1	NP12EHD2	NP12EHD3	NP12HD1	NP12HD2	NP12HD3				
NP12ED1	NP12ED2	NP12ED3	NP12D1	NP12D2	NP12D3				
NP2EHD1	N EHD2	NP2EHD3	NP2HD1	NP2HD2	NP2HD3				
NP2ED1	NP2ED2	NP2ED3	NP2D1	NP2D2	NP2D3				
MP12EHD1	MP12EHD2	MP12EHD3	MP12HD1	MP12HD2	MP12HD3	LP12HD1	LP12HD2	LP12HD3	LP12HD4
MP12ED1	MP12D2	MP12ED3	MP12D1	MP12D2	MP12D3	LP12D1	LP12D2	LP12D3	LP12D4
MP2EHD1	MP2EHD2	MP2EHD3	MP2HD1	MP2HD2	MP2HD3	LP2HD1	LP2HD2	LP2HD3	LP2HD4
MP2ED1	MP2ED2	MP2ED3	MP2D1	MP2D2	MP2D3	LP2D1	LP2D2	LP2D3	LP2D4

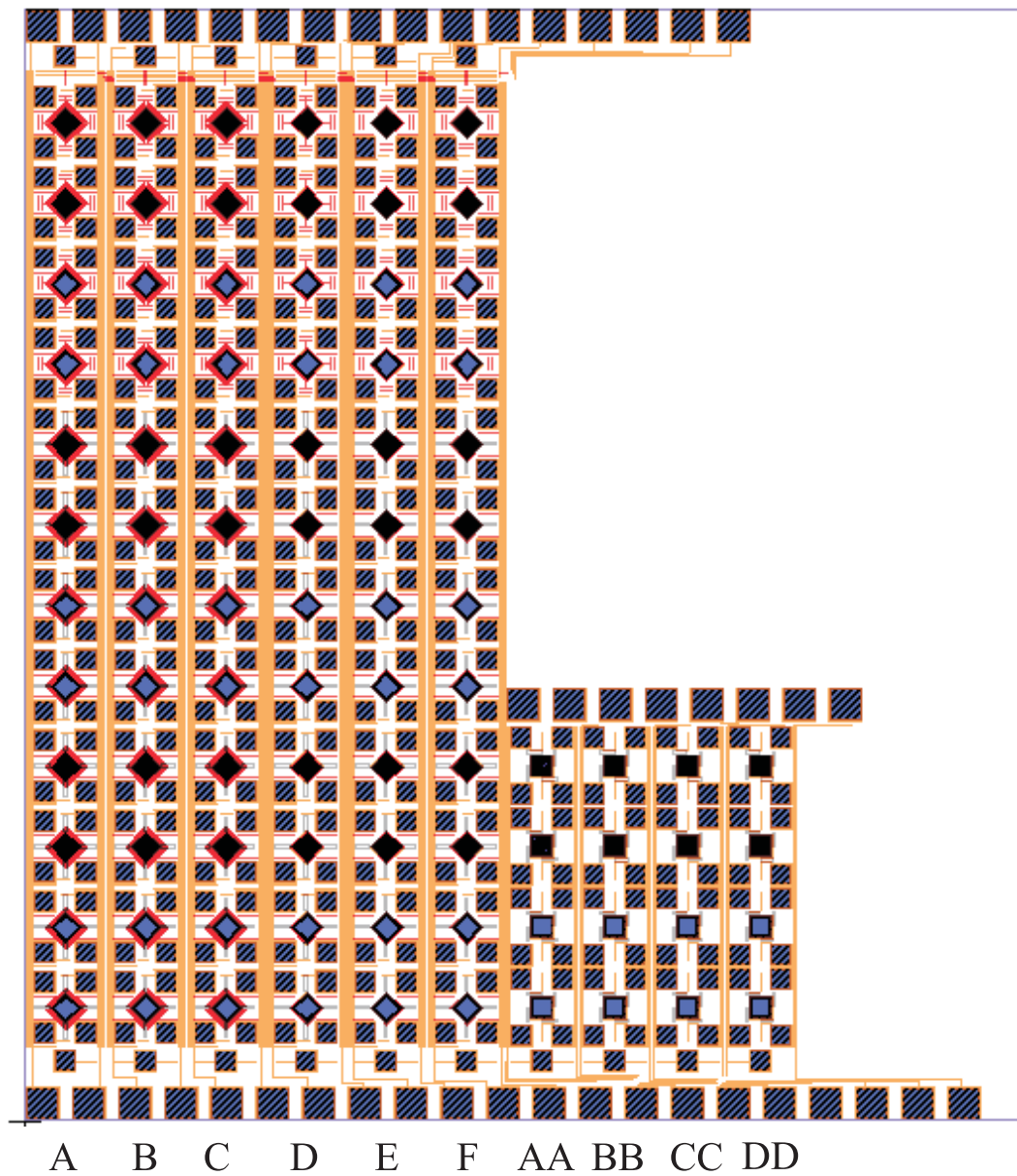


Figure 23: Layout for MUMPs run 39.

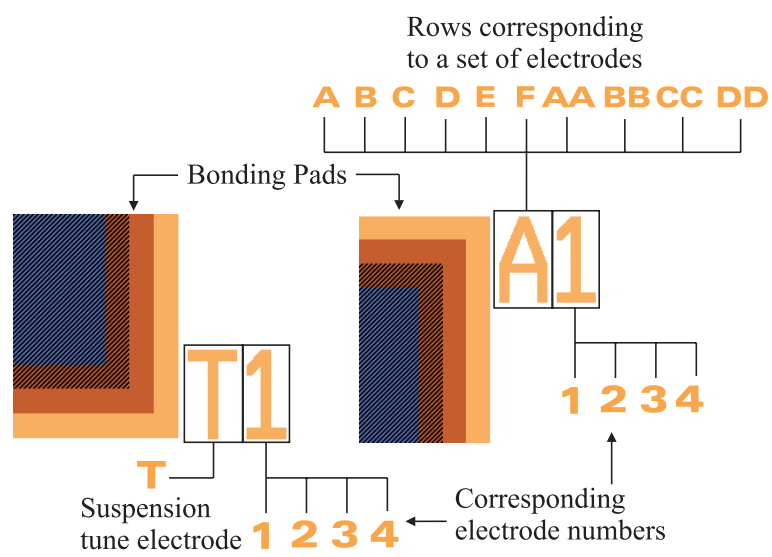


Figure 24: Bonding pad labels.